energies

MDPI

Article

Synergetic Effect of Non-Condensable Gas and Steam Quality on the Production Capacity of Geothermal Wells and Geothermal Power Generation for Hot Dry Rock

Tailu Li [1], Ruizhao Gao [1], Xiang Gao [1,*] and Qinghua Liu [2]

[1] School of Energy and Environmental Engineering, Hebei University of Technology, Tianjin 300401, China
[2] China Electronics System Engineering NO.2 Construction Co., Ltd., Wuxi 214111, China
* Correspondence: 2018020@hebut.edu.cn; Tel./Fax: +86-22-60435787

Abstract: This paper aims to fill the research gap on the effect of steam quality and non-condensable gas on heat-carrying fluid productivity, system performance and optimization. First, the effect of the temperature and quality of the heat-carrying fluid and non-condensable gas (NCG) content on the production parameters was evaluated. After that, three energy conversion systems which included a single flash (SF) system, an organic Rankine cycle (ORC) system and a single flash combined ORC (SFORC) system were constructed in this paper to utilize the heat-carrying two-phase flow with non-condensable gas. Finally, based on thermodynamic modeling, the effects of the temperature and quality of the heat-carrying fluid and non-condensable gas content on the performance and optimization of the three power conversion systems were investigated. The results show that single-phase heat-carrying fluids are more productive than two-phase heat-carrying fluids. NCG is always detrimental. The heat-carrying fluid temperature and quality are positively correlated with system efficiency and negatively correlated with the net power output. In the comparison of comprehensive performances, the SFORC system is the better, and the ORC system and the SF system are the worse. The optimal net power output of the SF system, the ORC system and the SFORC system is 4883 kW, 6557 kW and 7251 kW, respectively.

Keywords: production capacity of hot dry rock (HDR); heat-carrying two-phase fluid; steam quality; non-condensable gas (NCG); energy conversion systems

check for updates

Citation: Li, T.; Gao, R.; Gao, X.; Liu, Q. Synergetic Effect of Non-Condensable Gas and Steam Quality on the Production Capacity of Geothermal Wells and Geothermal Power Generation for Hot Dry Rock. *Energies* **2022**, *15*, 7726. https://doi.org/10.3390/en15207726

Academic Editor: Adrián Mota Babiloni

Received: 22 September 2022
Accepted: 17 October 2022
Published: 19 October 2022

Publisher's Note: MDPI stays neutral with regard to jurisdictional claims in published maps and institutional affiliations.

Copyright: © 2022 by the authors. Licensee MDPI, Basel, Switzerland. This article is an open access article distributed under the terms and conditions of the Creative Commons Attribution (CC BY) license (https://creativecommons.org/licenses/by/4.0/).

1. Introduction

The long-term fossil-dominated energy consumption structure has caused serious environmental pollution, and the transition to clean energy is increasingly urgent [1]. Geothermal resources have received the attention of scholars because of their abundant reserves and stable accessibility [2,3]. Hot dry rock (HDR) is more representative of geothermal exploitation and has been a hot spot in the development and utilization of geothermal energy resources around the world in recent years [4,5]. The enhanced geothermal system (EGS) which is used in the exploitation of HDR consists of two parts: the underground heat extraction system and the above-ground energy conversion system [6–9]. The heat-carrying fluid can be divided into three categories according to the phase state: hot water, vapor–liquid two-phase flow and dry steam [10]. Currently, most geothermal power plants are designed and optimized based on pure liquid-phase geothermal resources with temperatures below 200 °C [11–14]. However, in reality, some vapor fraction is often present in the heat-carrying fluid. In the Rangyi geothermal reservoir located in Tibet, the steam mass fraction is about 10% [15]. Many geothermal fields around the world produce geothermal fluids that contain non-condensable gas (NCG), such as the Kizildere geothermal field, the Broadlands-Ohaaki and Kawerau geothermal fields, the Aidlin geothermal project in The Geysers [16] and the Bagnore geothermal field [17]. NCG contains a variety of gases, of which CO_2 is the main component, and the proportion of CO_2 in NCG is usually greater

than 85% [18]; The proportion of CO_2 in NCG is from 96% to 99% in built geothermal power plants [19]. In the design of a geothermal power plant, the quality of the heat-carrying fluid and the proportion of NCG need to be carefully considered.

Mubarok et al. [20] used a computational fluid dynamics (CFD) model solved by ANSYS Fluent to simulate two-phase geothermal fluid flow in a production pipeline using six types of flow meters and then developed a CFD model to predict the fluid flow behavior. Mubarok et al. [21] analyzed field test data using load sensors from five different wells to investigate their possible application in estimating the enthalpy of the geothermal two-phase fluids. The fluid velocities were successfully predicted using cross-correlation techniques. However, in the absence of the slip ratio and void fraction, the enthalpy of the fluid cannot be measured using the liquid velocity alone. Hasan et al. [22] presented a robust model for a two-phase flow in geothermal wells using the drift-flux approach and compared it with the commonly used models. The new model offered greater accuracy and simplicity of use. Their work was limited to the underground heat extraction system and did not consider the effect of the heat-carrying fluid on the performance of the energy conversion system.

Nogara et al. [18] studied the corrosion resistance of nine types of carbon steels and corrosion-resistant alloys (CRA) in geothermal fluids with a high non-condensable gas content (NCG). Karabacak et al. [23] investigated the technique of using non-condensing gas which originates from a heat-carrying fluid containing 96% CO_2 to produce CO_2. It was found that the production cost of carbon dioxide from geothermal fluids is 13–20% cheaper than other methods. Manente et al. [24] analyzed and compared integrated flash-binary and two-phase binary layouts. The two plant layouts they considered integrated water absorption and the reinjection of H_2S and CO_2. Altar et al. [25] developed digital simulation techniques to study the effects of the reinjection of brine-containing dissolved NCG. The numerical simulations showed that minerals dissolve to a greater extent than they precipitate, leading to an increase in permeability and porosity. Although there are many studies related to non-condensable gases in heat-carrying fluids, the effect of non-condensable gases on energy conversion systems has been less studied.

The above-ground energy conversion system usually consists of a flash power generation system, binary cycle system, dry steam system and composite power generation system [10]. Flash power generation systems can be divided into the single flash (SF) system, the double flash (DF) system and the multiflash system (more than three) which has the worse economic performance. The organic Rankine cycle (ORC) as one of the binary cycle systems is widely promoted for its applicability to low- and medium-temperature heat sources [26,27]. The optimization and comparative studies of flash evaporation systems were carried out by Pambudi et al. [28], Rudiyanto et al. [29], Dagdas et al. [30], Parikhani et al. [31], Meng et al. [32] and Mohammadzadeh et al. [33]. Fang et al. [34], Wang et al. [35], Huang et al. [36], Li et al. [37] and Dawo et al. [38] have studied ORC systems in terms of working fluid selection, parameter optimization, structural improvement and experimental studies. Neither the above literature nor the composite power generation systems such as the SFORC and the DFORC studied by Aali et al. [39], Abdolalipouradl et al. [33] and Shokati et al. [40] consider the effect of the quality of the heat-carrying fluid as well as the non-condensable gas content.

Shamoushaki et al. [41] analyzed a conceptual geothermal power plant with NCG reinjection from an energy, exergy, economic and environmental perspective. Chen et al. [42] designed a network topology using open source Python thermal energy engineering system (TESPy) software to simulate the operation of an ORC plant using a vapor–liquid two-phase heat-carrying fluid and compared the performance of six different working fluids. The effect of the quality of the heat-carrying fluid on the performance of the four energy conversion systems which included a single flash (SF) system, a single flash combined ORC (SFORC) system, a double flash (DF) system and a double flash combined ORC (DFORC) system was investigated by Li et al. [43]. Only lower quality conditions were studied above,

and the effect of NCG on production capacity and the system performance of the operation parameters was not studied.

In this paper, we investigated the effect of heat-carrying fluids with a steam quality which was from 0 to 0.9 and an NCG volume rate which was from 0 to 5% at different temperatures on the production capacity, optimal operation parameters and performance of three energy conversion systems. The three energy conversion systems were an SF system, an ORC system and an SFORC system.

2. System Description

In this paper, three energy conversion systems were studied: an SF system, an ORC system and an SFORC system.

The schematic diagram of the SF system is shown in Figure 1a. Figure 1b shows the *T*-*s* diagram of the SF system. The high-temperature and high-pressure heat-carrying fluid which is heated by hot dry rock and comes from the wellhead of the production well is transported to the vapor–liquid separator to expand and depressurize (process 1–2 in Figure 1b). Then, the generated saturated vaporized heat-carrying fluid is delivered to the turbine to output mechanical power which is converted to electricity (process 4–5 in Figure 1b). The heat-carrying fluid vapor from the turbine outlet enters the condenser and is condensed by the cooling water (process 5–6 in Figure 1b). Finally, the liquid heat-carrying fluid from the condenser and vapor–liquid separator is pumped into the injection well and returned to the underground. A complete SF cycle is finished.

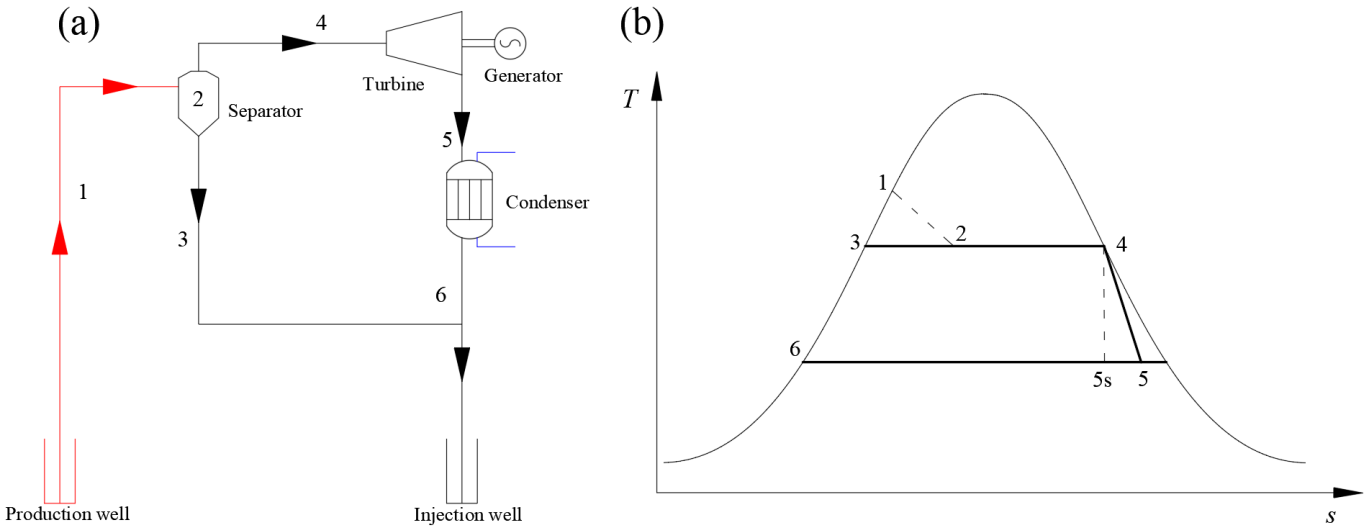


Figure 1. The schematic diagram and *T*-*s* diagram of the SF system (**a**) schematic diagram; (**b**) *T*-*s* diagram.

The schematic diagram and the *T*-*s* diagram of the ORC system are shown in Figure 2a,b, respectively. The high-temperature and high-pressure heat-carrying fluid which comes from the wellhead of the production well is cooled by the organic working fluid (process 8–4 in Figure 2b), and the resulting liquid heat-carrying fluid enters the injection well and returns to the subsurface. The working fluid vapor enters the turbine and drives the generator to generate electricity (process 4–5 in Figure 2b). The working fluid removed by the turbine is condensed by the cooling water in the condenser (process 5–7 in Figure 2b). The working fluid liquid is pumped into the evaporator to complete a cycle (process 7–8 in Figure 2b).

Figure 3 shows the schematic diagram and *T*-*s* diagram of the SFORC system. The SFORC system is a dual cycle system, consisting of two subsystems, an SF subsystem and an ORC subsystem. The high-temperature and high-pressure heat-carrying fluid is transported to the vapor–liquid separator to expand and depressurize, which is the same as process 1–2 in Figure 1b. Next, the generated saturated vaporized heat-carrying fluid is delivered to the turbine to output mechanical power, which is converted to electricity,

which is similar to process 4–5 in Figure 1b. The liquid heat-carrying fluid from the turbine outlet enters the evaporator of the ORC system and is condensed by the organic working fluid (process 11–7 in Figure 3b). Then, the working fluid vapor enters the turbine for power generation (process 7–8 in Figure 3b). The working fluid vapor is condensed in condenser 2 (process 8–10 in Figure 3b), then pressurized by the pump (process 10–11 in Figure 3b) and goes to the evaporator, while the vapor–liquid two-phase heating-carrying fluid is condensed in condenser 1, which is analogous to process 5–6 in Figure 1b and enters the injection well. At this point, the SFORC cycle is complete.

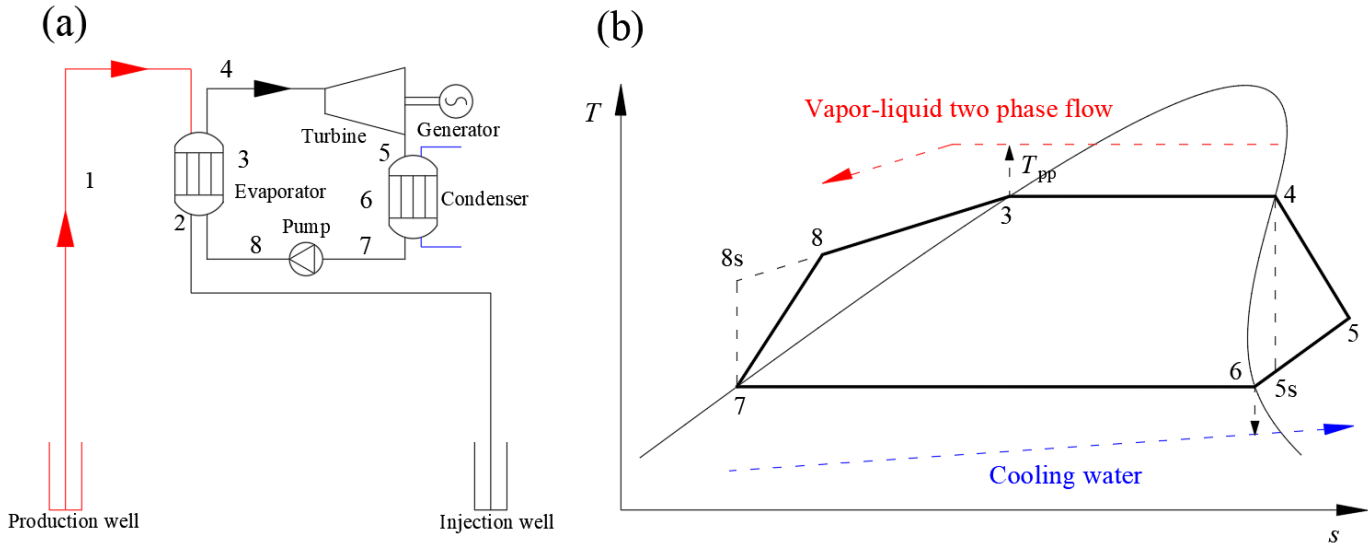


Figure 2. The schematic diagram and *T-s* diagram of the ORC system. (**a**) schematic diagram; (**b**) *T-s* diagram.

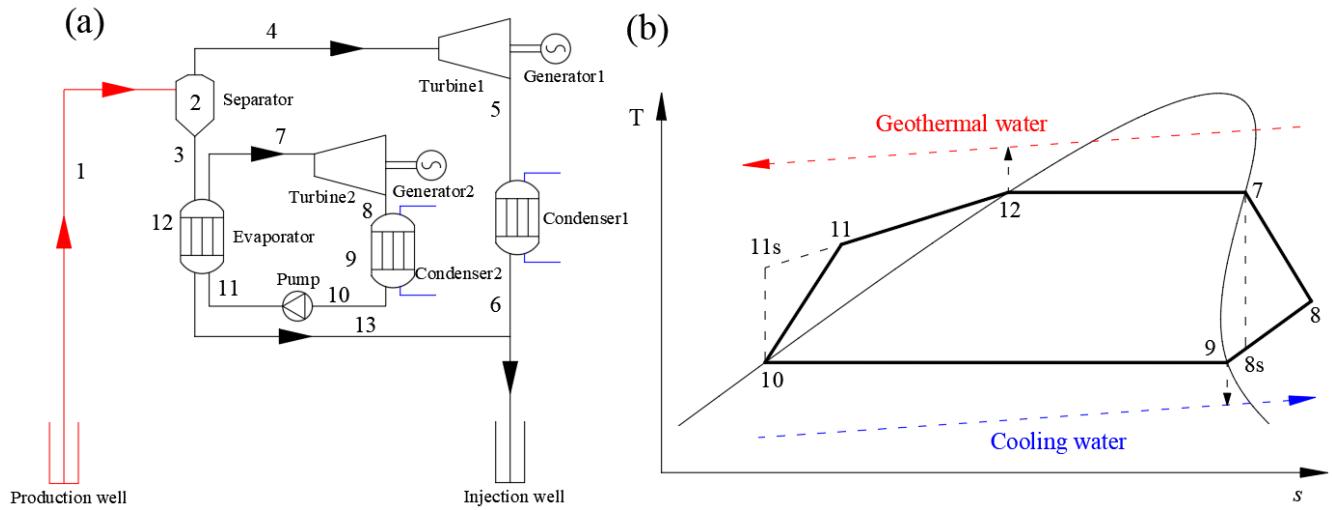


Figure 3. The schematic diagram and *T-s* diagram of the SFORC system. (**a**) schematic diagram; (**b**) *T-s* diagram.

3. Mathematical Model

To facilitate the thermodynamic modeling of the energy conversion systems, the following assumptions were made based on the first and second laws of thermodynamics:

(1) Systems are modeled under steady-state conditions [44];
(2) Changes in the kinetic and potential energy of organic working fluids in the system are ignored [45];

(3) The pressure drop and friction loss of working fluids in evaporators, condensers and pipes as well as heat losses in pipes are ignored because the pipes are insulated well [46];
(4) The working fluid at the inlet of the pump is in the saturated liquid state, and the working fluid at the inlet of the turbine is in a saturated vapor state;
(5) The temperature difference between the evaporation and condensation process of the ORC system is taken as 5 °C in this paper;
(6) The pressure range of the vapor–liquid separator in both the SF system and the SFORC system is $P_1 > P_2 > 1$ bar [47];
(7) The non-condensable gas is assumed to be pure CO_2 [23].

3.1. Mathematical Model of Heat-Carrying Fluid

The heat-carrying fluid is usually a multicomponent, vapor–liquid two-phase flow with non-condensable gas. Non-condensable gas contains a variety of gases, of which CO_2 is the main component, and the proportion of CO_2 in non-condensable gas is usually greater than 85%. The proportion of CO_2 in the non-condensable gas is found to be 96–99% in actual power plants. Therefore, it is assumed that the non-condensable gas is CO_2, and the volume share of CO_2 in the heat-carrying fluid is 0~5% in this paper.

Parameters such as heat-carrying fluid temperature, pressure and volumetric flow rate can be measured during the capacity test. However, the remaining parameters need to be calculated, and the parameters at the wellhead can be calculated as follows.

The mass flow rate of heat-carrying fluid:

$$m_{\mathrm{HCF}} = \frac{\rho_{\mathrm{HCF}} V_{\mathrm{HCF}}}{3600} = \frac{\rho_{\mathrm{w}} V_{\mathrm{w}} + \rho_{\mathrm{s}} V_{\mathrm{s}} + \rho_{\mathrm{CO2}} V_{\mathrm{CO2}}}{3600} \tag{1}$$

where m stands for the mass flow rate, ρ is density, and V represents the volume flow rate. The subscript "HCF", "s" and "w" mean the heat-carrying fluid, geothermal steam, and geothermal water, respectively.

The CO_2 share of heat-carrying fluid:

$$R_{\mathrm{CO2}} = \frac{V_{\mathrm{CO2}}}{V_{\mathrm{HCF}}} \tag{2}$$

where R_{CO2} is the ratio of CO_2 in the non-condensable gas.

The quality of heat-carrying fluid:

$$x_{\mathrm{HCF}} = \frac{m_{\mathrm{s}}}{m_{\mathrm{s}} + m_{\mathrm{w}}} \tag{3}$$

The specific enthalpy of the heat-carrying fluid:

$$h_{\mathrm{HCF}} = \frac{m_{\mathrm{w}} h_{\mathrm{w}} + m_{\mathrm{s}} h_{\mathrm{s}} + m_{\mathrm{CO2}} h_{\mathrm{CO2}}}{m_{\mathrm{HCF}}} \tag{4}$$

The specific entropy of the heat-carrying fluid:

$$s_{\mathrm{HCF}} = \frac{m_{\mathrm{w}} s_{\mathrm{w}} + m_{\mathrm{s}} s_{\mathrm{s}} + m_{\mathrm{CO2}} s_{\mathrm{CO2}}}{m_{\mathrm{HCF}}} \tag{5}$$

The enthalpy of the heat-carrying fluid at the wellhead:

$$H_{\mathrm{HCF}} = m_{\mathrm{HCF}} h_{\mathrm{HCF}} \tag{6}$$

The specific entropy and entropy of the heat-carrying fluid at the wellhead:

$$ex_{\mathrm{HCF}} = h_{\mathrm{HCF}} - h_0 - T_0(s_{\mathrm{HCF}} - s_0) \tag{7}$$

$$EX_{HCF} = m_{HCF} ex_{HCF} \tag{8}$$

3.2. Mathematical Model of the SF System

The following mathematical model of the SF system was developed according to the schematic diagram in Figure 1a.

Vapor–liquid separator:

$$h_1 = h_2 \tag{9}$$

$$m_1 = m_2 + m_3 + m_{CO2} \tag{10}$$

$$m_1 h_1 = m_2 h_2 + m_3 h_3 + m_{CO2} h_{CO2,t4} \tag{11}$$

Turbine:

$$\eta_{T,SF} = \frac{h_4 - h_5}{h_4 - h_{5s}} \tag{12}$$

$$m_4 = m_5 \tag{13}$$

$$W_{T,SF} = (m_4 + m_{CO2})(h_{mix4} - h_{mix5}) \tag{14}$$

where $W_{T,\,SF}$ is the turbine power output.

Condenser:

$$m_5 = m_6 \tag{15}$$

$$Q_{C,SF} = (m_5 + m_{CO2}) h_{mix5} - m_6 h_6 - m_{CO2} h_{CO2,t6} \tag{16}$$

where $Q_{C,\,SF}$ stands for the heat exchange of the SF condenser.

The net power output of the SF system:

$$W_{net,\,SF} = \eta_T W_{T,\,SF} - W_{cp,\,SF} - W_{HCF,\,SF} \tag{17}$$

where η_T represents the isentropic efficiency of the turbine, and W_{CP} and W_{HCF} stand for the power consumption of the cooling water circulation pump and heat-carrying fluid circulation pump, respectively.

The energy efficiency of the SF system:

$$\eta_{th,\,SF} = \frac{W_{net,\,SF}}{Q_{HCF,\,SF}} \times 100\% \tag{18}$$

where $\eta_{th,\,SF}$ is the energy efficiency of the SF system, and $Q_{HCF,\,SF}$ means the energy of the heat-carrying fluid utilized by the SF system.

The exergy efficiency of the SF system:

$$\eta_{ex,\,SF} = \frac{W_{net,\,SF}}{EX_{HCF,\,SF}} \times 100\% \tag{19}$$

where $\eta_{ex,\,SF}$ is the exergy efficiency of the SF system, and $EX_{HCF,\,SF}$ means the exergy of the heat-carrying fluid utilized by the SF system.

3.3. Mathematical Model of the ORC System

The mathematical modeling of the ORC system was developed as follows:

Evaporator:

$$Q_{E,ORC} = m_{HCF}(h_{HCF,in} - h_{HCF,out}) = m_{wf,ORC}(h_4 - h_8) \tag{20}$$

where $Q_{E,\,SFORC}$ is the heat exchange of the evaporator for the ORC system.

Turbine:

$$W_{T,ORC} = m_{wf,ORC}(h_4 - h_5) \tag{21}$$

where $W_{T,\,ORC}$ represents the power output of the turbine for the ORC system.

Condenser:

$$Q_{\mathrm{C,ORC}} = m_{\mathrm{wf,ORC}}(h_5 - h_7) \tag{22}$$

where $Q_{\mathrm{C,\,ORC}}$ stands for the heat exchange of the condenser for the ORC system.

Cooling water pump:

$$W_{\mathrm{cp,ORC}} = \frac{m_{\mathrm{cw,ORC}} g H_{\mathrm{cp}} \rho_{\mathrm{cw}}}{\eta_{\mathrm{cp}}} \tag{23}$$

where $W_{\mathrm{cp,\,ORC}}$ means the power consumption of the cooling water pump.

Working fluid pump:

$$W_{\mathrm{wp,ORC}} = m_{\mathrm{wf,ORC}}(h_8 - h_7) \tag{24}$$

where $W_{\mathrm{wp,\,ORC}}$ means the power consumption of the working fluid pump.

The mass flow rate of the working fluid:

$$m_{\mathrm{wf,ORC}} = \frac{m_{\mathrm{HCF,ORC}}(h_{\mathrm{HSF,in}} - h_{\mathrm{HSF,out}})}{h_4 - h_8} \tag{25}$$

The net power output of the ORC system:

$$W_{\mathrm{net,\,ORC}} = \eta_{\mathrm{T}} W_{\mathrm{T,\,ORC}} - W_{\mathrm{cp,\,ORC}} - W_{\mathrm{HCF,\,ORC}} - W_{\mathrm{wp,ORC}} \tag{26}$$

where $W_{\mathrm{net,\,ORC}}$ stands for the net power output of the ORC system.

The energy efficiency of the ORC system:

$$\eta_{\mathrm{th,\,ORC}} = \frac{W_{\mathrm{net,\,ORC}}}{Q_{\mathrm{HCF,\,ORC}}} \times 100\% \tag{27}$$

where $\eta_{\mathrm{th,\,ORC}}$ is the energy efficiency of the ORC system, and $Q_{\mathrm{HCF,\,ORC}}$ means the energy of the heat-carrying fluid utilized by the ORC system.

The exergy efficiency of the ORC system:

$$\eta_{\mathrm{ex,\,ORC}} = \frac{W_{\mathrm{net,\,ORC}}}{EX_{\mathrm{HCF,\,ORC}}} \times 100\% \tag{28}$$

where $\eta_{\mathrm{ex,\,ORC}}$ is the exergy efficiency of the ORC system, and $EX_{\mathrm{HCF,\,ORC}}$ means the exergy of the heat-carrying fluid utilized by the ORC system.

3.4. Mathematical Model of the SFORC System

The mathematical modeling of the flash portion of the SFORC system is consistent with the SF system, and this section only mathematically models the ORC subsystem of the SFORC.

Evaporator:

$$Q_{\mathrm{E,SFORC}} = m_{\mathrm{HCF}}(h_{\mathrm{HCF,3}} - h_{\mathrm{HCF,out}}) = m_{\mathrm{wf,SFORC}}(h_7 - h_{11}) \tag{29}$$

where $Q_{\mathrm{E,\,SFORC}}$ is the heat exchange of the evaporator for the ORC subsystem.

Turbine:

$$W_{\mathrm{T2,SFORC}} = m_{\mathrm{wf,SFORC}}(h_7 - h_8) \tag{30}$$

where $W_{\mathrm{T2,\,SFORC}}$ represents the power output of the turbine2 for the ORC subsystem.

Condenser:

$$Q_{\mathrm{C2,SFORC}} = m_{\mathrm{wf,SFORC}}(h_8 - h_{10}) \tag{31}$$

where $Q_{\mathrm{C2,\,SFORC}}$ stands for the heat exchange of condenser2 for the ORC subsystem.

Cooling water pump:

$$W_{\text{cp2, SFORC}} = \frac{m_{\text{cw2}} g H_{\text{cp}} \rho_{\text{cw}}}{\eta_{\text{cp}}} \tag{32}$$

where W_{cp} means the power consumption of the cooling water pump.

Working fluid pump:

$$W_{\text{wp,SFORC}} = m_{\text{wf,SFORC}}(h_{11} - h_{10}) \tag{33}$$

where $W_{\text{wp, SFORC}}$ means the power consumption of the working fluid pump.

The mass flow rate of the working fluid:

$$m_{\text{wf,SFORC}} = \frac{c_{\text{HCF,SFORC}} m_{\text{HCF,SFORC}}(t_3 - t_{12} - \Delta t_{\text{pp}})}{h_7 - h_{12}} \tag{34}$$

where Δt_{pp} is the pinch point temperature of the evaporation process.

The net power output of the SFORC system:

$$W_{\text{net, SFORC}} = \eta_{\text{T}} W_{\text{T, SFORC}} - W_{\text{cp, SFORC}} - W_{\text{HCF, SFORC}} - W_{\text{wp, SFORC}} \tag{35}$$

where $W_{\text{net, SFORC}}$ stands for the net power output of the SFORC system.

The energy efficiency of the SFORC system:

$$\eta_{\text{th, SFORC}} = \frac{W_{\text{net, SFORC}}}{Q_{\text{HCF, SFORC}}} \times 100\% \tag{36}$$

where $\eta_{\text{th, SFORC}}$ is the energy efficiency of the SFORC system, and $Q_{\text{HCF, SFORC}}$ means the energy of the heat-carrying fluid utilized by the SFORC system.

The exergy efficiency of the SFORC system:

$$\eta_{\text{ex, SFORC}} = \frac{W_{\text{net, SFORC}}}{EX_{\text{HCF, SFORC}}} \times 100\% \tag{37}$$

where $\eta_{\text{ex, SFORC}}$ is the exergy efficiency of the SFORC system, and $EX_{\text{HCF, SFORC}}$ means the exergy of the heat-carrying fluid utilized by the SFORC system.

4. Validation

The SF system model is validated by similar previous studies [48]. Table 1 shows that the results have a good agreement in comparison with the published date which uses the same working fluid under the same temperature of the heat-carrying fluid at the inlet and flash temperature. The mathematical model of the ORC system is validated by the results of Saleh et al. The comparison shows a good agreement between this paper and the results of reference [49] as shown in Table 2. $m_{\text{r_ORC}}$ refers to the mass flow rate referring to a power output of 1 MW.

Table 1. Comparative results of SF system between this paper and a previous study.

State	Working Fluid	*T* (K)		*p* (MPa)		*h* (kJ/kg)	
		Present Study	Ref. [48]	Present Study	Ref. [48]	Present Study	Ref. [48]
1(E1)	water	573.2	573.2	8.840	8.584	1344	1344
2(E2)	water	488.2	488.2	0.8918	0.8918	1344	1344
3(E7)	water	488.2	488.2	0.8918	0.8918	741.2	741.2
4(E3)	water	488.2	488.2	0.8918	0.8918	2773	2773
5(E4)	water	323.1	323.1	0.01234	0.01234	2285	2253
6(E8)	water	411.05	411.9	0.3404	0.3489	580.3	584.0

Table 2. Comparative results of ORC system between this paper and a previous study.

Substance	$t_{HCF,\ in}$ (°C)	t_e (°C)	$t_{HCF,\ out}$ (°C)	p_{max} (MPa)	m_{r_ORC} (kg/s)	η_{th} (%)	Source
R245fa	120.0	110.0	50.70	1.269	33.80	11.98	Present study
				1.267	33.42	12.52	Ref. [49]

5. Results and Discussion

Heat-carrying fluid is usually a multicomponent, vapor–liquid two-phase flow with partially non-condensable gas. The non-condensable gas contains a variety of gases, of which CO_2 is the main component and is assumed to be pure CO_2. Considering the geological conditions and the hot dry rock resources in China, the volume share of CO_2 in the heat-carrying fluid is assumed to be 0~5% in this paper.

5.1. Synergetic Effect on Production Capacity

5.1.1. Under a Fixed Volume Flow Rate

The volume flow rate of the heat-carrying fluid at the wellhead is assumed to be 100 m^3/h in this subsection.

Figure 4 shows the variation curves of the production capacity parameters with the different temperatures and steam quality of the heat-carrying fluid without non-condensable gas. Figure 4a shows the trend of the mass flow rate of the heat-carrying fluid under different qualities and temperatures. As the temperature of the heat-carrying fluid increases, the mass flow rate of the heat-carrying fluid, whose quality is 0, is decreasing, while the mass flow rate of the heat-carrying fluid with a quality of 0.1 to 0.9 is increasing. This is due to the increment of the temperature of the heat-carrying fluid reducing the density of the heat-carrying fluid when the steam quality is 0, while the increase in the temperature of the heat-carrying fluid makes the density decrease when the quality is from 0.1 to 0.9. Under the condition of the constant temperature of the heat-carrying fluid, the mass flow rate of the heat-carrying fluid corresponding to the quality of 0 is always the maximum value and is much higher than the mass flow rate under the rest of the quality conditions; therefore, it can be concluded that the smaller the steam quality, the higher the mass flow rate of the heat-carrying fluid. When the steam quality is from 0 to 0.3, the effect of the quality on the mass flow rate is more obvious, while the effect of the quality on the mass flow rate is smaller when the steam quality is from 0.4 to 0.9, and the change in mass flow rate gradually decreases. For example, at a heat-carrying fluid temperature of 200 °C, the quality varies from 0 to 0.1, and the heat-carrying fluid mass flow rate varies from 24.02 kg/s to 2.02 kg/s, which relatively decreases by 91.6%. The steam quality changes from 0.5 to 0.6, and the heat-carrying fluid mass flow rate changes from 0.43 kg/s to 0.36 kg/s, with a relative decrease of 16.3%. Under the same heat-carrying fluid temperature, the steam quality change leads to the change in the percentage of the vapor and liquid phase of the heat-carrying fluid, while the density of the vapor is smaller than that of the liquid, and the mass flow rate at a high steam quality is smaller than the mass flow rate at a low quality. The higher the temperature of the heat-carrying fluid, the slower the growth of the mass flow rate of the heat-carrying fluid under the same steam quality. For example, at the steam quality of 0.1, the mass flow rate of the heat-carrying fluid increases from 0.17 kg/s to 0.23 kg/s, which is relatively increased by 26.1%, when the temperature increases from 100 °C to 110 °C; while the mass flow rate of the heat-carrying fluid increases from 1.67 kg/s to 2.02 kg/s, which is relatively increased by 17.33%, when the temperature increases from 190 °C to 200 °C. Under the same quality conditions, changes in the temperature of the heat-carrying fluid only affect the density of the heat-carrying fluid, which, in turn, affects the mass flow rate of the heat-carrying fluid.

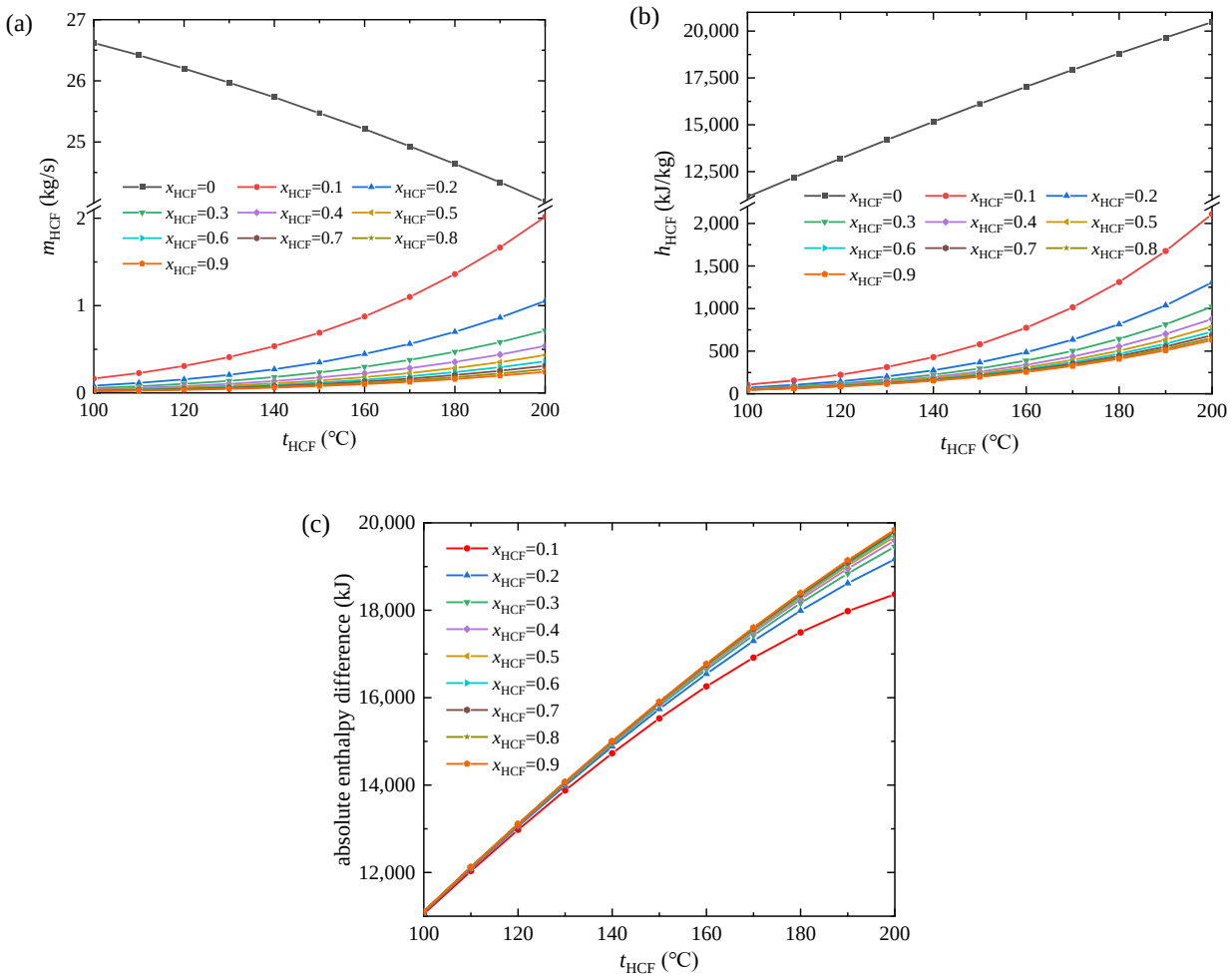


Figure 4. Variation curves of production capacity parameters of heat carrier with t_{HCF} under the different steam quality: (**a**) mass flow rate, (**b**) enthalpy and (**c**) absolute enthalpy difference.

The variation of the heat-carrying fluid enthalpy at the wellhead with the temperature under a different quality is shown in Figure 4b. When the quality is 0, the variation of the enthalpy with temperature is the opposite of the trend of the mass flow rate, while the steam quality is from 0.1 to 0.9, and the variation of the enthalpy with temperature is the same as the mass flow rate. The enthalpy and quality are negatively correlated at a certain temperature of the heat-carrying fluid. The enthalpy at the wellhead is affected by both the mass flow rate and the specific enthalpy of the heat-carrying fluid. When the quality is 0, the increase rate of the specific enthalpy is much larger than the decrease rate of the mass flow rate; therefore, the enthalpy, when the quality is 0, shows an increasing trend. When the steam quality is from 0.1 to 0.9, both the mass flow rate and specific enthalpy increase with the temperature, and as a result, the enthalpy keeps increasing. Figure 4c displays the variation of the absolute enthalpy difference with the temperature of the heat-carrying fluid under different steam quality when vapor is neglected and the heat-carrying fluid is assumed to be only hot water.

The absolute enthalpy difference and temperature of the heat-carrying fluid are positively correlated with different steam quality, and the larger the quality, the greater the absolute enthalpy difference. The greater the steam quality, the smaller the enthalpy at the wellhead and the larger the enthalpy difference at the wellhead between the pure hot water and vapor–liquid two-phase heat-carrying fluid. Therefore, there will be a large error if simplifying the heat-carrying fluid type from a vapor–liquid two-phase flow to a single liquid.

Figure 5 displays the variation curves of the production capacity parameters at different temperatures and the non-condensable gas rate of the heat-carrying fluid. As shown in Figure 5a, the correlation between the mass flow rate and temperature of the heat-carrying fluid is negative, while the mass flow rate and R_{CO2} are also negatively correlated. The mass flow rate of the heat-carrying fluid always reaches the maximum value when the temperature is 100 °C with fixed R_{CO2}. The mass flow rate of the heat-carrying fluid is 26.62 kg/s at the heat-carrying fluid temperature of 100 °C and R_{CO2} of 0. The mass flow rate of the heat-carrying fluid with R_{CO2} of 5% is 25.29 kg/s, which is a reduction of 1.33 kg/s. For example, the mass flow rate of the heat-carrying fluid changes from 26.36 kg/s to 23.79 kg/s when the heat-carrying fluid temperature range is 100 °C to 200 °C and R_{CO2} is equal to 1%. The mass flow rate decreases by 2.57 kg/s. The effect of the heat-carrying fluid temperature on the mass flow rate is more significant compared to R_{CO2}.

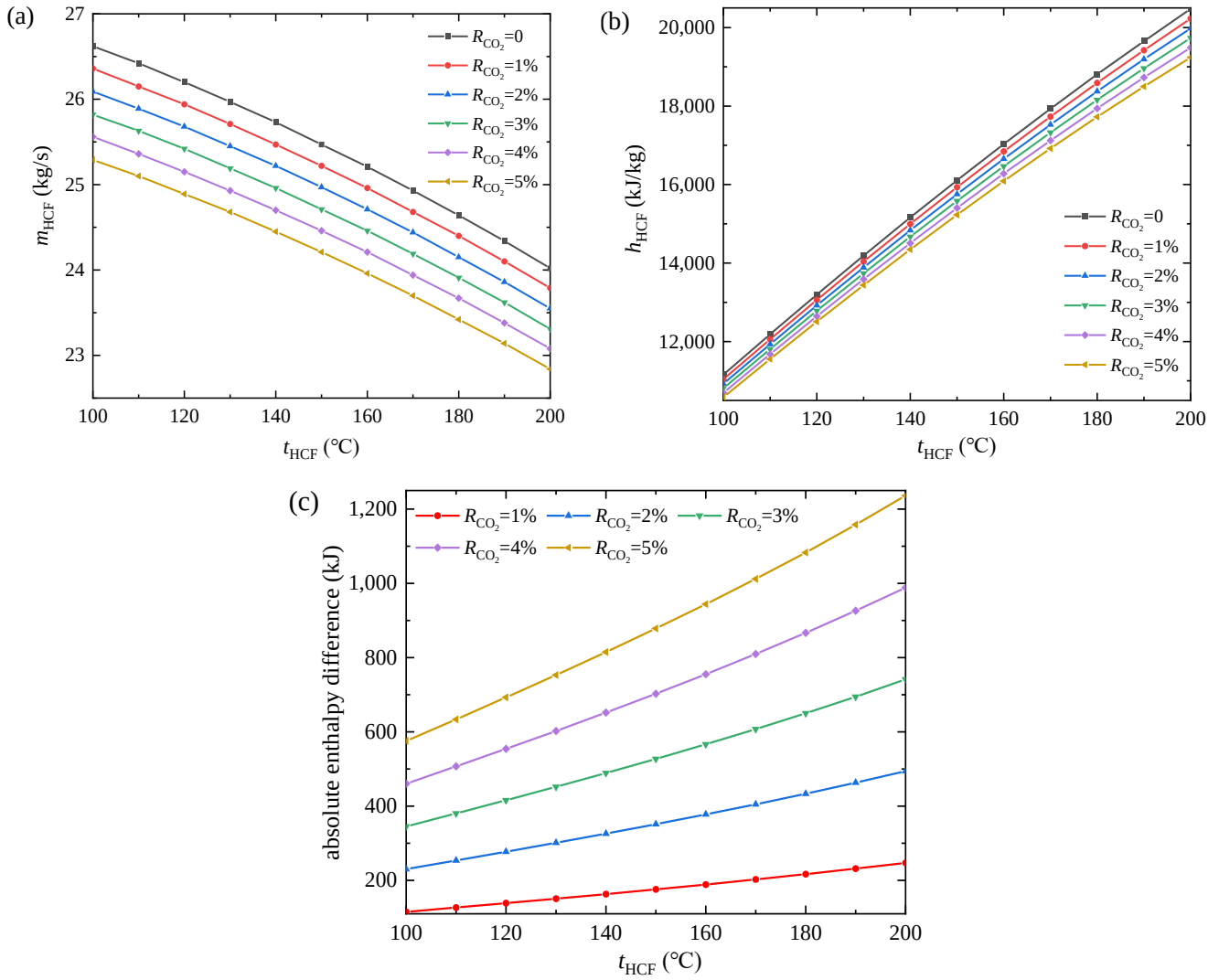


Figure 5. Variation curves of productivity parameters of heat carrier with t_{HCF} under different R_{CO2}: (**a**) mass flow rate, (**b**) enthalpy and (**c**) absolute enthalpy difference.

The enthalpy of the heat-carrying fluid at the wellhead is positively correlated with temperature, while it is negatively correlated with R_{CO2}, which can be seen in Figure 5b. When the temperature of the heat-carrying fluid is 100 °C, the enthalpy decreases by about 1% for every increment in R_{CO2} of 1%; when the temperature of the heat-carrying fluid is 200 °C, the enthalpy decreases by about 1.3% for every increment in R_{CO2} of 1%. At the same steam quality, the higher the temperature of the heat-carrying fluid, the greater the effect of R_{CO2} on the enthalpy at the wellhead. Figure 5c shows the trend of the absolute

enthalpy difference with the temperature of the heat-carrying fluid at different R_{CO2} when the non-condensable gas content is neglected. At a heat-carrying fluid temperature of 200 °C, the absolute enthalpy differences are 247.1 kJ and 1236 kJ when R_{CO2} is 1% and 5%, respectively.

At a higher temperature, the greater the R_{CO2}, the greater the absolute enthalpy difference, while the rate of change in the absolute enthalpy difference corresponding to different R_{CO2} does not significantly change as the temperature of the heat-carrying fluid increases.

Figure 6 demonstrates the synergetic effect of the steam quality and R_{CO2} on the productivity parameters at a temperature of 180 °C. In Figure 6a, the mass flow rate of the heat-carrying fluid is negatively correlated with R_{CO2} with a quality of 0–0.4, while it is positively correlated with R_{CO2} when the steam quality is 0.4–0.9. The detailed data are shown in Table 3. When the quality is 0~0.4, the increment of R_{CO2} has a greater effect on the mass flow rate of the vapor–liquid two-phase flow, and the sum of the mass flow rate of the vapor–liquid two-phase flow and the mass flow rate of CO_2 gradually decreases, which makes the mass flow rate of the heat-carrying fluid show a decreasing trend. While the steam quality is 0.5~0.9, the effect of R_{CO2} on the mass flow rate of the vapor–liquid two-phase flow is smaller; therefore, the increment of R_{CO2} makes the mass flow rate of the heat-carrying fluid show an increasing trend. In Figure 6c, the smaller the steam quality and the larger the R_{CO2}, the larger the absolute enthalpy difference. The absolute enthalpy difference is 1083 kJ for the quality of 0 and R_{CO2} of 5%.

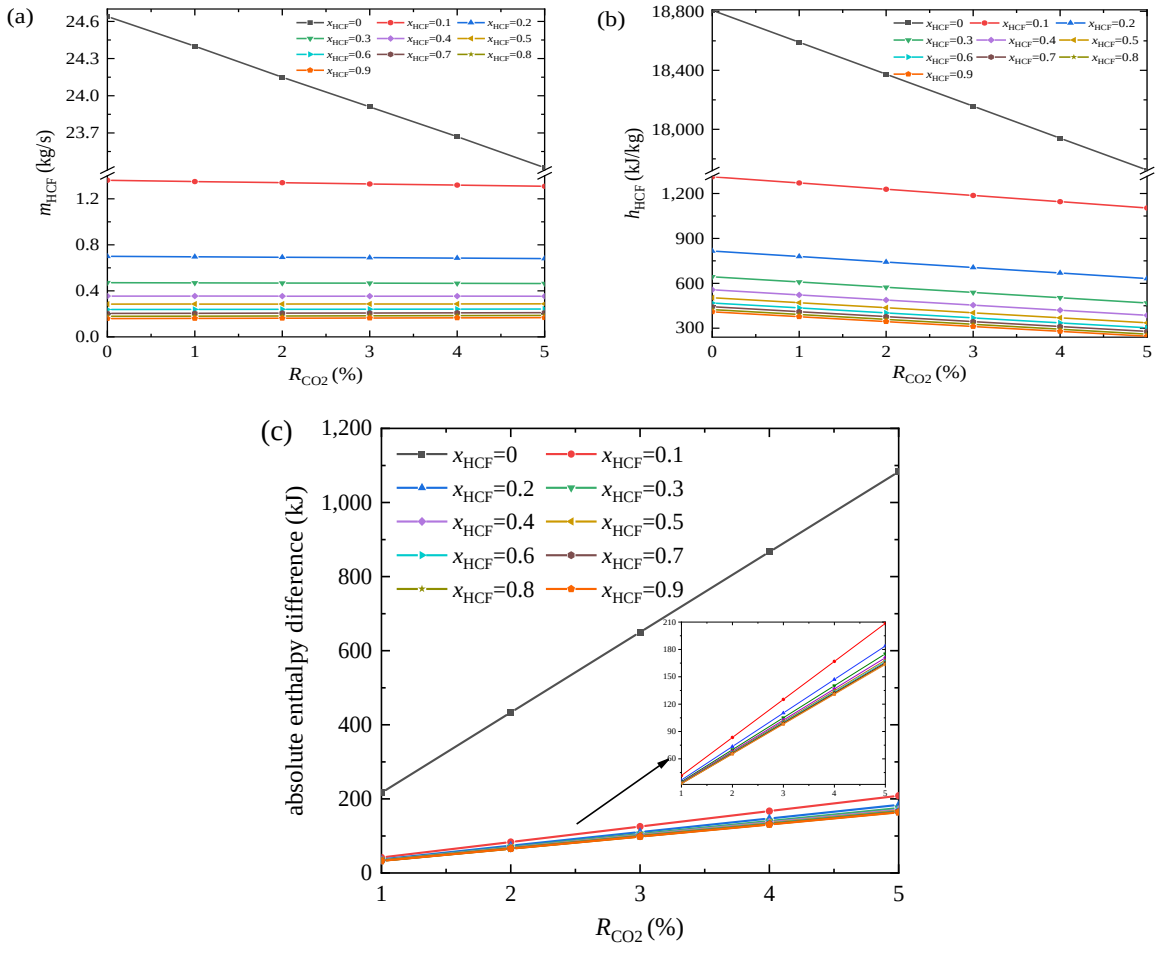


Figure 6. Variation curves of wellhead productivity parameters of heat carrier with R_{CO2} under different steam quality: (**a**) mass flow rate, (**b**) enthalpy and (**c**) absolute enthalpy difference.

Table 3. The mass flow rate of heat-carrying fluid under different steam quality.

R_{CO2} (%)	m_{HCF} (kg/s) (x_{HCF} = 0)	m_{HCF} (kg/s) (x_{HCF} = 0.4)	m_{HCF} (kg/s) (x_{HCF} = 0.5)	m_{HCF} (kg/s) (x_{HCF} = 0.9)
0	24.64	0.3548	0.2847	0.1590
1	24.40	0.3545	0.2851	0.1606
2	24.15	0.3542	0.2855	0.1623
3	23.91	0.3539	0.2859	0.1640
4	23.67	0.3536	0.2863	0.1656
5	23.42	0.3533	0.2867	0.1673

5.1.2. Under a Fixed Mass Flow Rate

The mass flow rate of the heat-carrying fluid at the wellhead is assumed to be 100 kg/s in this subsection.

The variation curves of the production capacity parameters with different temperatures and quality of heat-carrying fluid without non-condensable gas are illustrated in Figure 7a. The volume flow rate of the heat-carrying fluid is positively correlated with temperature at the quality of 0. The specific volume is positively correlated with temperature at the quality of 0. The correlation between the volume flow rate and temperature is positive under a fixed mass flow rate, while the volume flow rate of the heat-carrying fluid is negatively correlated with the temperature because the correlation between the specific volume rate and temperature is negatively correlated. The volume flow rate of the heat-carrying fluid is positively correlated with the steam quality. The greater the steam quality, the smaller the density of the heat-carrying fluid and the larger the volume flow rate under a constant temperature of the heat-carrying fluid. The specific enthalpy of the heat-carrying fluid is positively correlated with temperature and quality. As a result, the temperature and quality of the heat-carrying fluid are both positively correlated with the enthalpy of the heat-carrying fluid, which is shown in Figure 7b. As shown in Figure 7c, the absolute enthalpy difference is negatively correlated with the temperature, while it is positively correlated with the steam quality. The greater the steam quality, the large the enthalpy difference between the two-phase flow and the saturated liquid; therefore, the correlation between the absolute enthalpy difference and the steam quality is positive. The increment of the specific enthalpy of the two-phase flow is much smaller with the temperature increase, while the increment of the specific enthalpy of the saturated liquid is almost fixed. Hence, the absolute enthalpy difference is negatively correlated with temperature under a fixed mass flow rate.

Figure 8 displays the effect of the temperature of the heat-carrying fluid and non-condensable gas content on the production capacity parameters when the quality of heat-carrying fluid is 0. In addition, the heat-carrying fluid temperature is 180 °C. The volume flow rate is positively correlated with the non-condensable gas content. Although CO_2 is soluble in water, it is not easily soluble in water. The increase in non-condensable gas content necessarily leads to an increase in the volume flow rate. The correlation between the enthalpy of the heat-carrying fluid and the non-condensable gas content is negative because the enthalpy of CO_2 is lower than zero, which is shown in Figure 8b1,b2, especially in Figure 8b2. The density of CO_2 is lower than geothermal water; hence, the mass flow rate of CO_2 is smaller than geothermal water under the same temperature and pressure. As a result, the difference in enthalpy caused by non-condensable gas is not obvious enough. The absolute enthalpy difference of the heat-carrying fluid and non-condensable gas is negatively correlated. The specific enthalpy difference between CO_2 and water under the same temperature is gradually growing with the rising temperature. Therefore, the more non-condensable gas content, the greater the absolute enthalpy difference of the heat-carrying fluid.

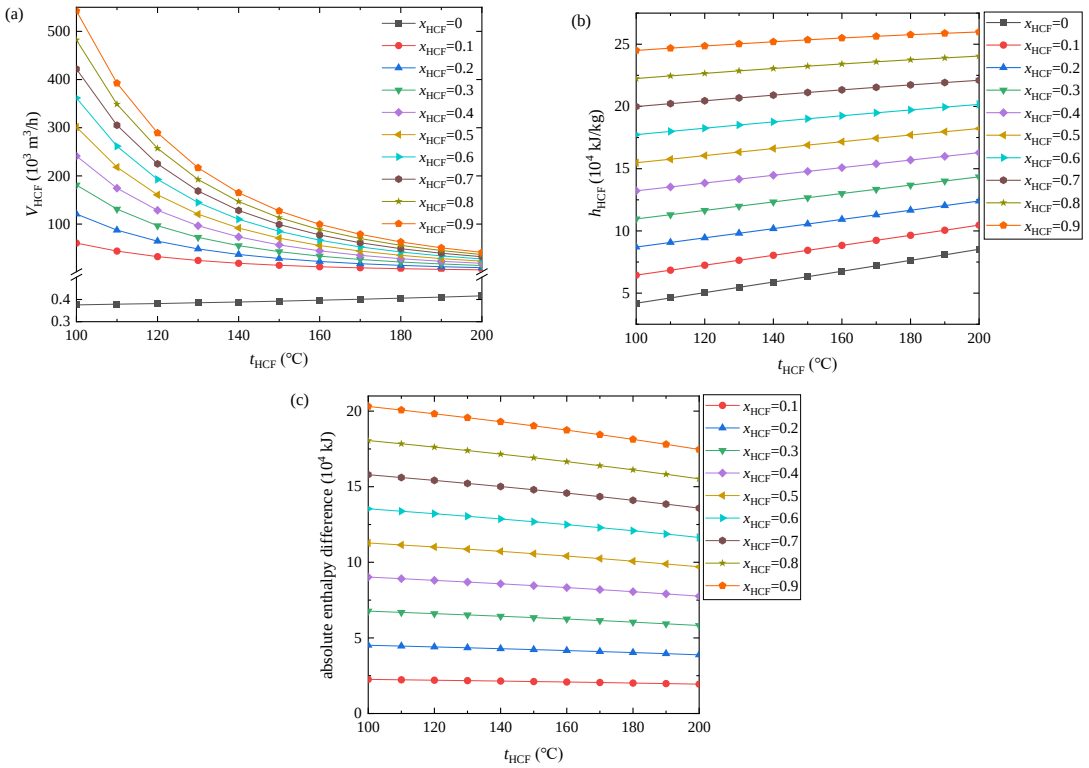


Figure 7. Variation curves of production capacity parameters of heat carrier with t_{HCF} under different qualities: (**a**) volume flow rate, (**b**) enthalpy and (**c**) absolute enthalpy difference.

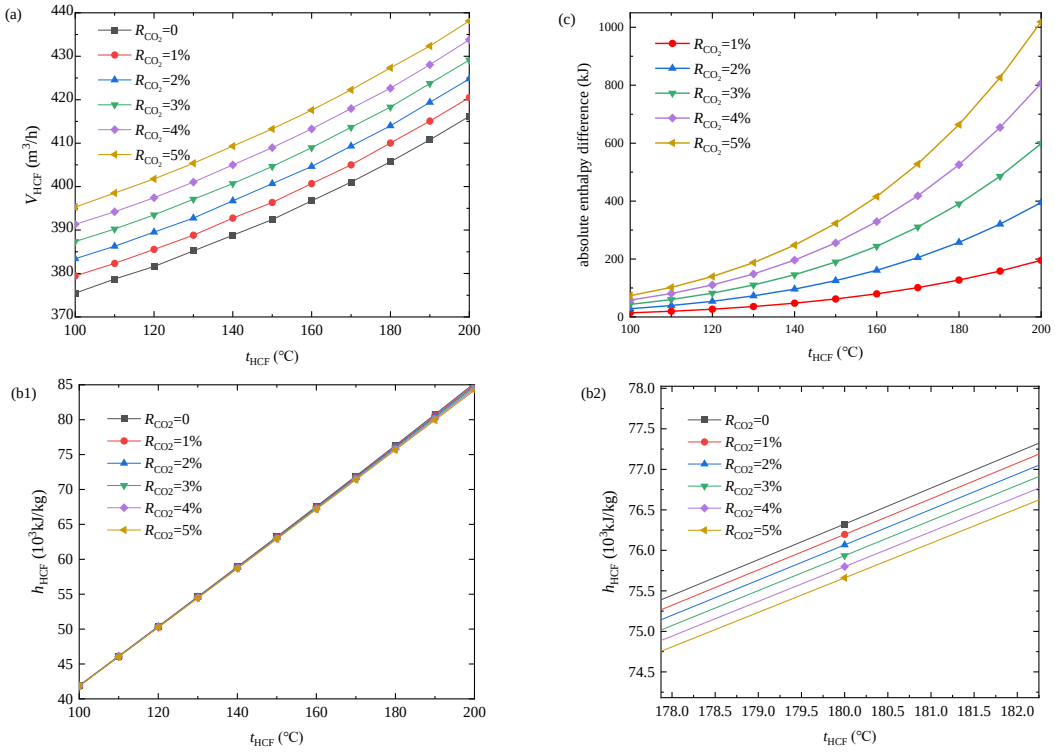


Figure 8. Variation curves of productivity parameters of heat carrier with t_{HCF} under different R_{CO2}: (**a**) volume flow rate, (**b1**,**b2**) enthalpy and (**c**) absolute enthalpy difference.

The synergetic effect of steam quality and R_{CO2} on the productivity parameters at a temperature of 180 °C is demonstrated in Figure 9. The volume flow rate of heat-carrying fluid is mainly determined by the steam quality. The effect of R_{CO2} on the volume flow rate is only more obvious when the steam quality is equal to 0. This is due to the fact that CO_2 is not easily soluble in water, and it is not difficult to mix with the unsaturated vapor. In addition, the volume flow rate of the heat-carrying fluid is positively correlated with the steam quality under a fixed mass flow rate. When the quality of the heat-carrying fluid is constant under the negative enthalpy of CO_2, the increase in the non-condensable gas content causes the enthalpy of the heat-carrying fluid to decrease, which is shown in Figure 9b. The greater the steam quality, the larger the specific enthalpy of the heat-carrying fluid, and the easier to reduce the negative impact of CO_2 enthalpy and the difference between the actual enthalpy of the heat-carrying fluid and enthalpy after simplification whose phase is a single liquid and no non-condensable gas. Thus, the absolute enthalpy difference is negatively correlated with the steam quality, while the correlation between the absolute enthalpy difference and steam quality is positive because there is no latent heat of vaporization available at the single liquid phase of the heat-carrying fluid.

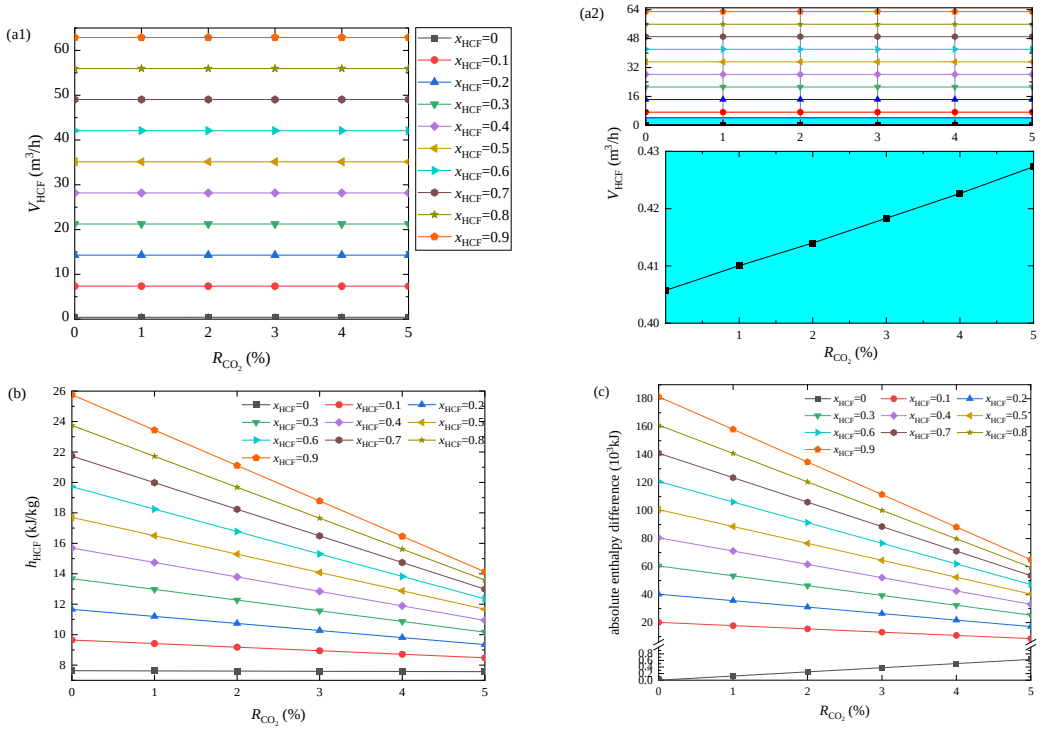


Figure 9. Variation curves of wellhead productivity parameters of heat carrier with R_{CO2} under different steam quality: (**a1**,**a2**) mass flow rate, (**b**) enthalpy and (**c**) absolute enthalpy difference.

5.1.3. Under a Fixed Heat Extraction

The heat extraction rate is assumed to be 2000 kW in this subsection [50].

Figure 10 shows the variation curves of the production capacity parameters with different temperatures and steam quality of the heat-carrying fluid without non-condensable gas. The temperature of the heat-carrying fluid is negatively correlated with the volume flow rate and mass flow rate because the increment in the temperature of the heat-carrying fluid makes the specific enthalpy of the heat-carrying fluid increase and the mass flow rate decrease when the quality is constant. At the same temperature, if the steam quality of the heat-carrying fluid rises, both the density and mass flow rate will decrease, and the rate of decline of the former is greater than that of the latter. As a result, the volume flow rate is positively correlated with the quality. As shown in Figure 10d, at a fixed steam quality, the specific enthalpy is increased, and the mass flow rate decreases as the temperature grows. Due to the correlation between the latent heat of vaporization and temperature

being negative, the error generated by neglecting the quality is reduced; therefore, the absolute enthalpy difference is negatively correlated with temperature. In contrast to this, the greater the steam quality, the greater the specific enthalpy error generated by neglecting the quality and the larger the absolute enthalpy difference. Consequently, the absolute enthalpy difference and steam quality are positively correlated.

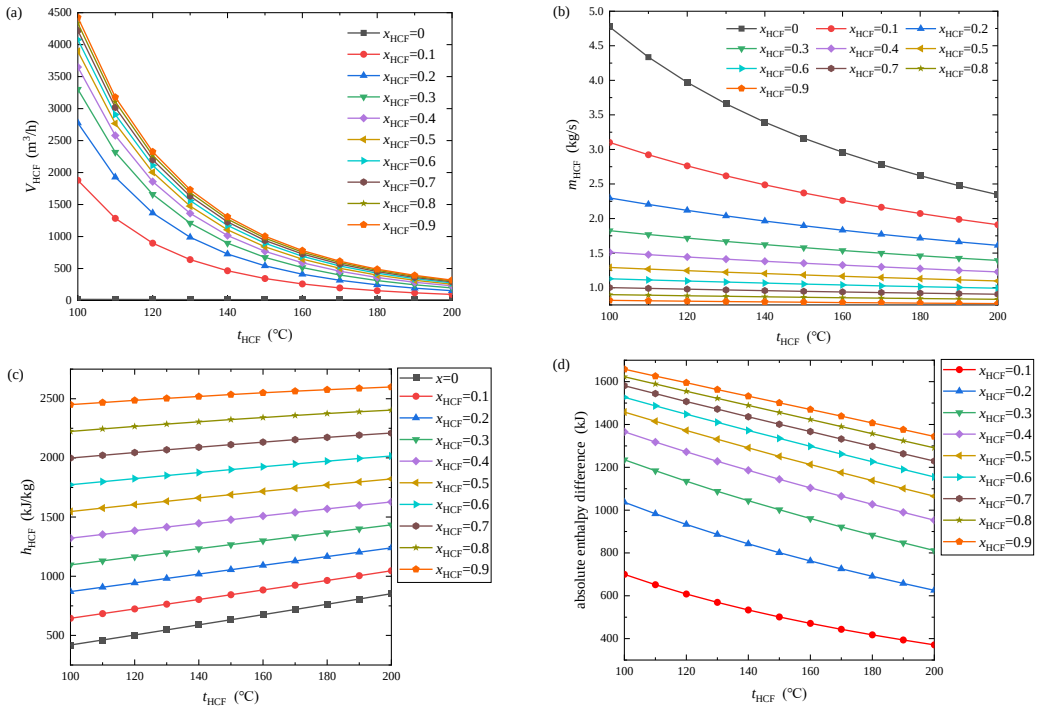


Figure 10. Variation curves of production capacity parameters of heat carrier with t_{HCF} under different steam quality: (**a**) volume flow rate, (**b**) mass flow rate, (**c**) enthalpy and (**d**) absolute enthalpy difference.

Figure 11 displays the variation curves of the production capacity parameters with different temperatures and non-condensable gas content of the heat-carrying fluid whose steam quality is 0. When the heat-carrying fluid is pure liquid, whose density is greater than CO_2, the non-condensable gas content is always negatively correlated with the mass flow rate and positively correlated with the volume flow rate. As a result, the bigger the non-condensable gas content, the smaller the mass flow rate, the greater the specific enthalpy and the larger the absolute enthalpy difference.

The synergetic effect of the steam quality and R_{CO2} on the productivity parameters at a temperature of 180 °C is demonstrated in Figure 12. When the heat-carrying fluid is pure liquid, whose density is bigger than CO_2, the higher the R_{CO2} and the greater the volume flow rate, whereas if the heat-carrying fluid is liquid–vapor two-phase flow, the volume flow rate will not obviously increase because volume cannot be directly added. With the gradual increase in steam quality, the density of unsaturated vapor gradually decreases; with the steam quality of a ($0.4 < a < 0.5$), the density of unsaturated vapor and the density of carbon dioxide are equal. Consequently, when the steam quality is from 0 to 0.4, the R_{CO2} and mass flow rate are negatively correlated, the correlation between R_{CO2} and the specific enthalpy is positive, and R_{CO2} is positively correlated with the absolute enthalpy difference. If the steam quality is from 0.5 to 0.9, and the R_{CO2} and mass flow rate are positively correlated, the correlation between R_{CO2} and specific enthalpy is negative, and R_{CO2} is negatively correlated with the absolute enthalpy difference.

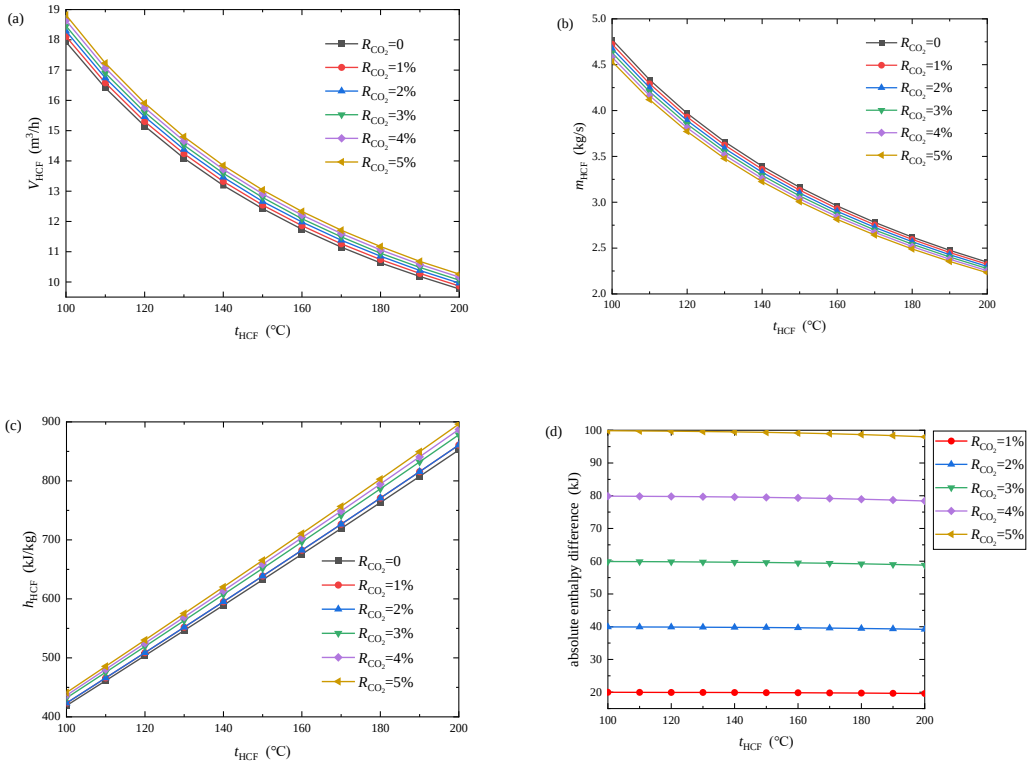


Figure 11. Variation curves of production capacity parameters of heat carrier with t_{HCF} under different R_{CO2}: (**a**) volume flow rate, (**b**) mass flow rate, (**c**) enthalpy and (**d**) absolute enthalpy difference.

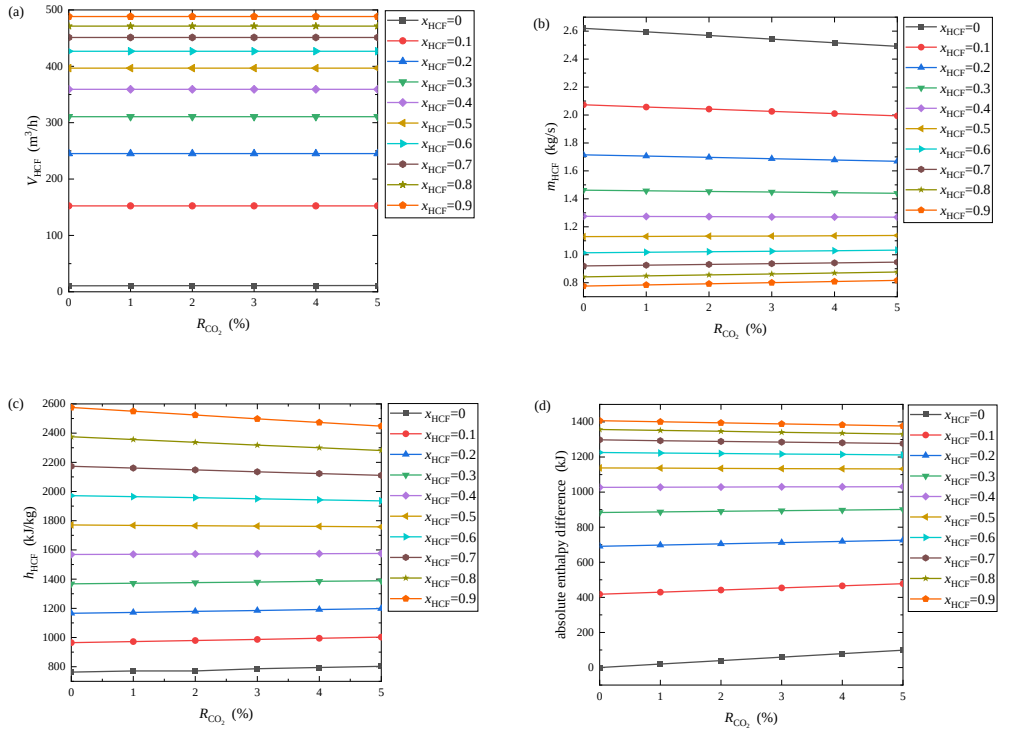


Figure 12. Variation curves of production capacity parameters of heat carrier with R_{CO2} under different steam quality: (**a**) volume flow rate, (**b**) mass flow rate, (**c**) enthalpy and (**d**) absolute enthalpy difference.

5.2. Comparison and Optimization of Power Generation Performance

The heat-carrying fluid temperature influences the system performance by affecting the circulation parameters; the higher the heat source temperature, the higher the upper limit of the evaporation temperature. In this subsection, the evaporation temperature or flash temperature is optimized to gain the optimal value of the net power output, which is recommended as the single objective optimization function [51].

A research well with a volume flow rate of about 360 m^3/h was studied in a geothermal field in the Tibet Autonomous Region, where the average annual temperature is 5 °C, and the average atmospheric pressure is 58.9 kPa. R601 was chosen as the working fluid for the ORC, and the thermophysical properties are shown in Table 4. Other simulation parameters are shown in Table 5.

Table 4. The thermophysical properties of R601 [52].

Substance	*M* (kg/mol)	t_b (°C)	t_{cri} (°C)	P_{cri} (MPa)	ODP	GWP (100 yr)
R601	72.15	36.00	196.50	3.37	0	~20

Table 5. Relevant parameters of the energy conversion system.

Parameter	Value	Parameter	Value
t_{HCF} (°C)	100–200	η_T (%)	75
V_{HCF} (m^3/h)	360	η_{hp}/η_{cp} (%)	75
R_{CO2} (%)	0~5	η_P (%)	60
X	0~0.9	η_F (%)	75
t_c (°C)	20	t_{pp} (°C)	5
$t_{cw,\,in}$ (°C)	6	η_m (%)	98
$t_{cw,\,out}$ (°C)	16	η_G (%)	97

Taking the example of the heat-carrying fluid temperature of 170 °C, the steam quality of 0 and R_{CO2} of 5%, the variation of the net power output for the three energy conversion systems is shown in Figure 13. The increase in the evaporation or flash temperature increases the specific enthalpy drop of the turbine on the one hand and reduces the mass flow rate of the working fluid on the other. As a result, there is maximum turbine power output. For the SF system, the higher the flash temperature, the less the mass flow rate of vapor, the less the mass flow rate of cooling water and the smaller the power consumption of the cooling water pump. Under the fixed condenser temperature and the same heat-carrying fluid, the power consumption of the heat-carrying fluid circulation pump is unchanged. Although the energy consumption is decreasing, the change in the turbine power output dominates as the net power output. Therefore, there is the maximum value of net power output of the SF system. Similarly, the turbine power output of the ORC system is at its maximum with the evaporation temperature rising, and the power consumption of the working fluid circulation pump is also decreasing. The correlation between the net power output and evaporation temperature is similar to the correlation between the turbine power output and the evaporation temperature. The SFORC system is the combination of the SF system and ORC system based on energy cascade utilization. Therefore, during the increase in evaporation or the flash temperature, there is the maximum value of the net power output of the three energy conversion systems.

Figure 14 shows the optimal cycle parameters corresponding to the optimal net power output for the three energy conversion systems at different temperatures and the steam quality of the heat-carrying fluid at R_{CO2} of 5%. In addition, the optimal cycle parameters corresponding to the optimal net power output at different heat-carrying fluid temperatures and at an R_{CO2} quality of 0.1 is displayed in Figure 15. When the quality is lower, the optimal flash/evaporation temperature and heat-carrying fluid temperature is positively correlated, while the optimal flash/evaporation temperature is fixed at a high enough quality. The higher the steam quality, the longer the isothermal heat transfer process and

the smaller the difference between the optimal evaporation temperature of the ORC system and the heat source temperature; however, the two are never the same due to the pinch point temperature limitation, whereas the optimal flash temperature can be equal to the heat source temperature. In the process of the flash/evaporation temperature converging to the optimal value, the exergy loss of heat exchange between the heat source and working fluid is reduced, and the system performance is improved. As shown in Figure 15, a change in R_{CO2} did not cause a change in the optimal flash/evaporation temperature because the increase in R_{CO2} only reduces the mass flow rate of the heat source and does not affect the heat source temperature.

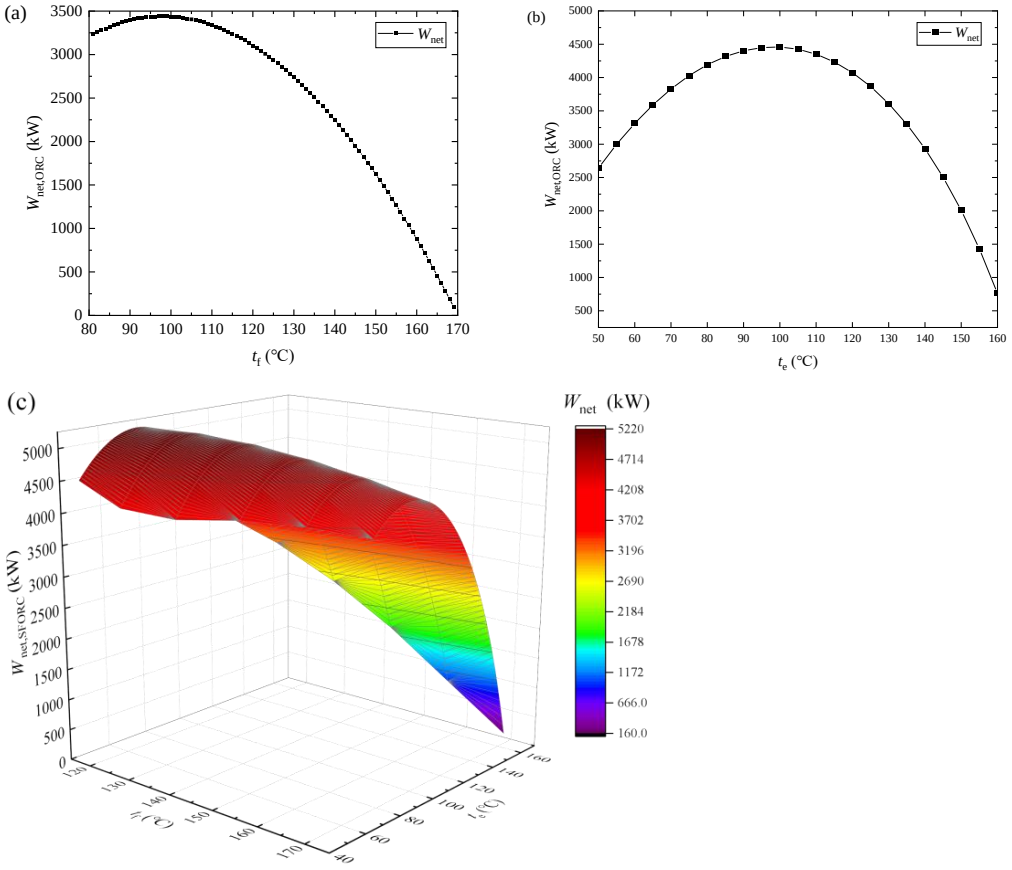


Figure 13. Variation trend of W_{net} of three energy conversion systems: (**a**) SF system, (**b**) ORC system and (**c**) SFORC system.

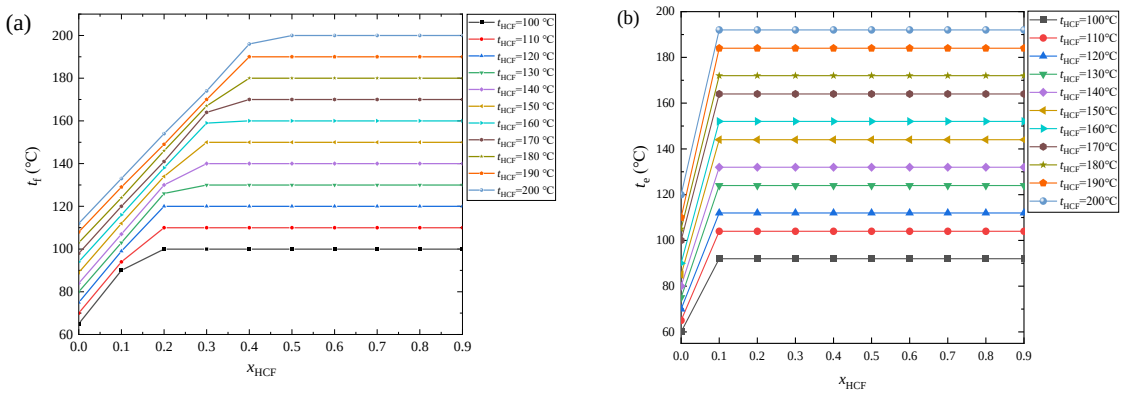


Figure 14. *Cont.*

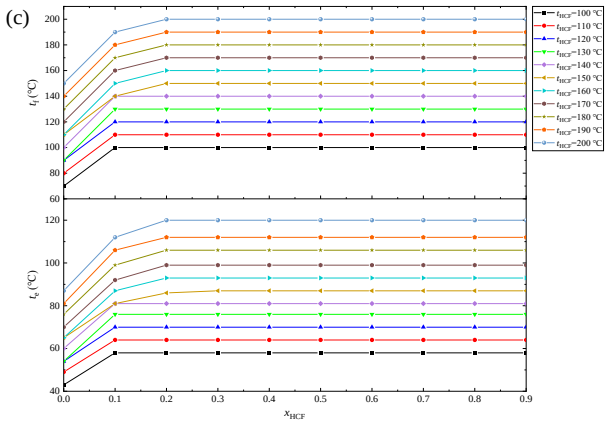


Figure 14. Optimal flash/evaporation temperature corresponding to the optimal W_{net} under different steam quality and temperatures of heat-carrying fluid: (**a**) SF system, (**b**) ORC system and (**c**) SFORC system.

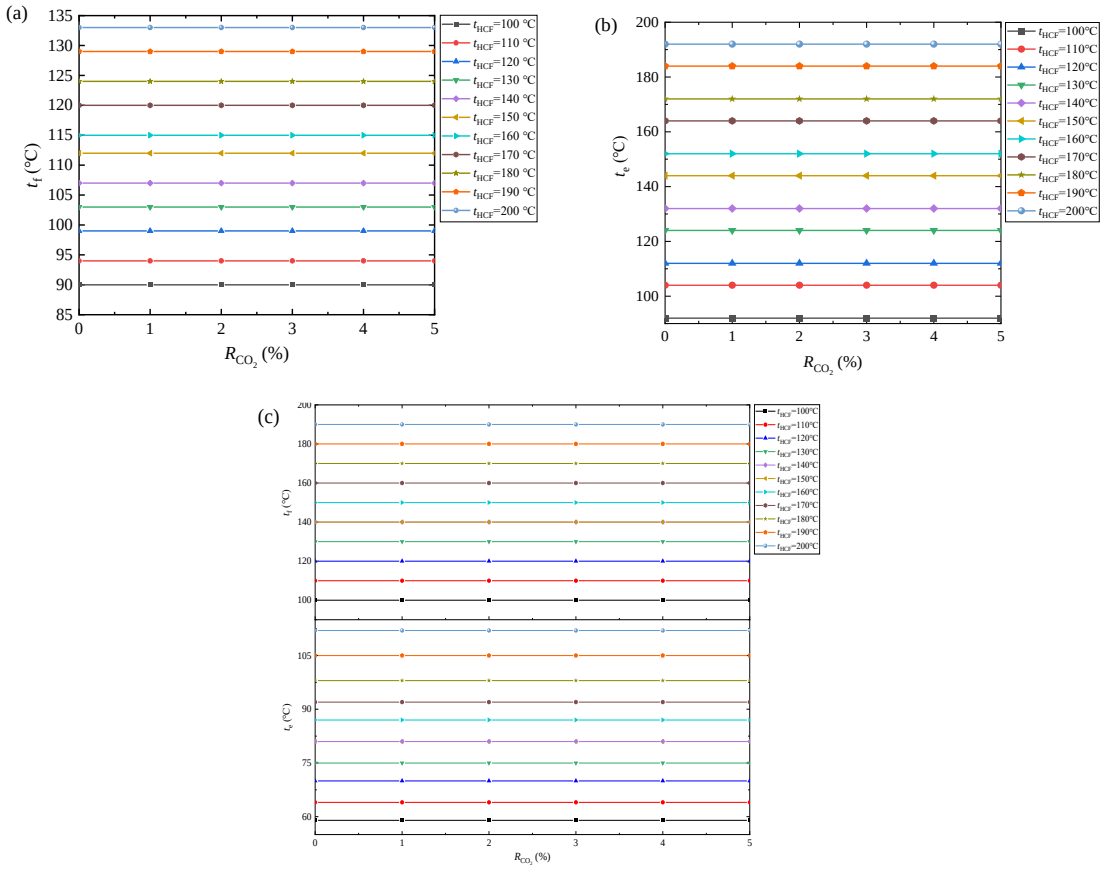


Figure 15. Optimal flash/evaporation temperature corresponding to the optimal W_{net} under different R_{CO2} and temperatures of heat-carrying fluid: (**a**) SF system, (**b**) ORC system and (**c**) SFORC system.

5.3. Synergetic Effect on Energy Conversion System Performance

In this subsection, the effect of the different heat-carrying fluid temperatures and different steam quality on the optimal thermal parameters of the three energy conversion systems is discussed with R_{CO2} assumed to be 5%.

5.3.1. Effect of Steam Quality on the System Performance

Figure 16 shows the variation curves of the optimal thermodynamic parameters of the SF system at different heat-carrying fluid temperatures and quality. In Figure 16a, the

net power output of the SF system and quality is a negative correlation, while the net power output is positively correlated with the heat-carrying fluid temperature. Taking the heat-carrying fluid temperature of 200 °C as an example, the quality changes from 0 to 0.1, and $W_{net,\,SF}$ decreases from 4883 kW to 649.6 kW, and the lower the temperature of the heat-carrying fluid, the greater the decrement of $W_{net,\,SF}$. This is because the increase in quality causes a rapid decrease in the density of the heat-carrying fluid and, consequently, in the mass flow rate of the heat-carrying fluid, as confirmed in Figure 15a. When the quality is 0, the increase in the temperature of the heat-carrying fluid reduces the mass flow rate of the heat-carrying fluid. However, it increases the specific enthalpy difference between the turbine inlet and outlet, and the rate of increase in the enthalpy difference between the turbine inlet and outlet is greater than the rate of decrease in the mass flow rate of the heat-carrying fluid. As a result, the net power output is positively correlated with the temperature of the heat-carrying fluid when the quality is 0. While the steam quality is 0.1~0.9, the increase in heat-carrying fluid temperature increases the mass flow rate of the heat-carrying fluid and the difference of enthalpy between the turbine inlet and outlet, so the $W_{net,\,SF}$ gradually increases with the increase in the heat-carrying fluid temperature. In Figure 16b, the thermal efficiency of the SF system gradually increases with the increase in the heat-carrying fluid temperature. Except for the quality of 0, the thermal efficiency of the SF system under the steam quality of 0.1~0.9 is approximated to gather into a curve. Under the same working condition, the thermal efficiency of the SF system with a steam quality of 0.1~0.9 is about 3% higher than the thermal efficiency with a quality of 0. In Figure 16c, both the temperature and the steam quality of the heat-carrying fluid are positively correlated with the exergy efficiency of the SF system. The increase in steam quality increases the optimal flash temperature, which, in turn, increases the recharge temperature of the heat-carrying fluid, and the difference between the inlet and outlet of the heat-carrying fluid becomes smaller, and the exergy efficiency of the SF system increases.

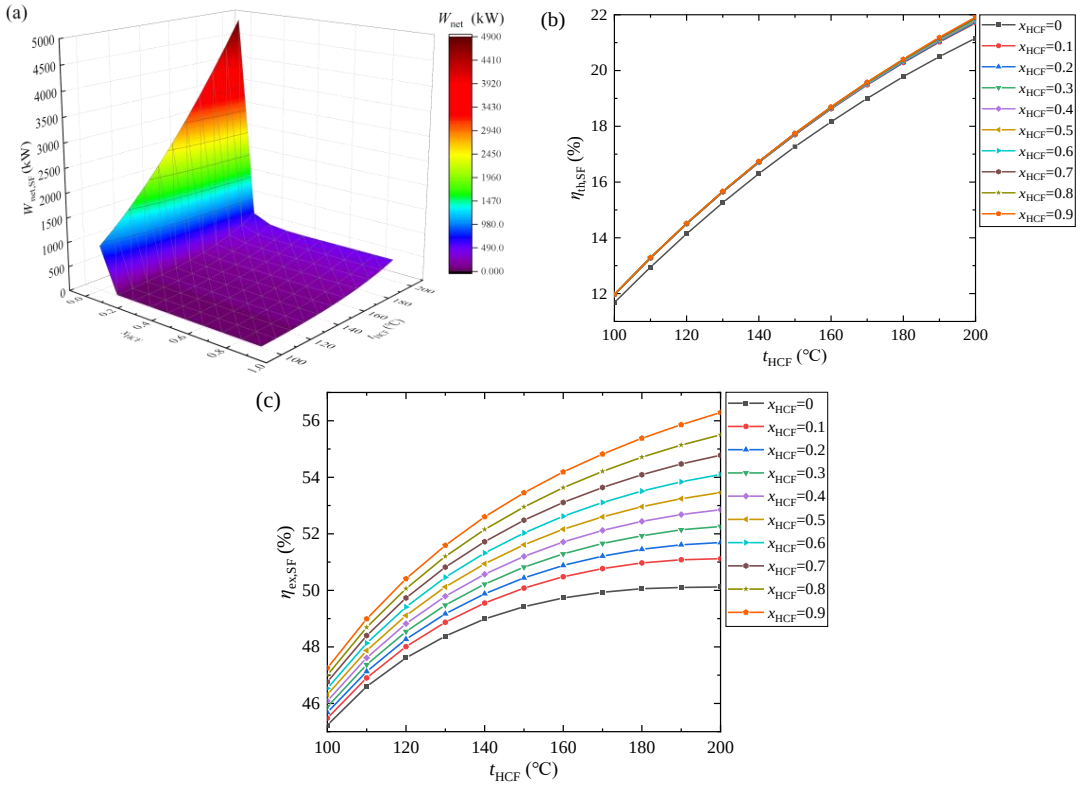


Figure 16. Variation of optimal thermodynamic parameters of the SF system with steam quality at different heat carrier temperatures: (**a**) $W_{net,\,SF}$, (**b**) $\eta_{th,\,SF}$ and (**c**) $\eta_{ex,\,SF}$.

Figure 17 shows the variation curves of the optimal thermodynamic parameters of the ORC system both at different temperatures and qualities of the heat-carrying fluid. As shown in Figure 17a, the net power output of the ORC system is positively correlated with the temperature of the heat-carrying fluid, while it is negatively correlated with the quality. In the case of certain steam quality, both the density and mass flow rate of the heat-carrying fluid are constant; an increase in the heat-carrying fluid temperature increases the amount of thermal energy available to the ORC system, increasing the net power output. The increment in quality causes a decrease in both the density and mass flow rate of the heat-carrying fluid. The heat absorption of the working fluid will also be reduced when the temperature of the heat-carrying fluid is fixed. The difference in the thermal efficiency of the ORC corresponding to the steam quality of 0~0.9 is smaller, and the thermal efficiency and heat-carrying fluid temperature are positively correlated. The effect of the heat-carrying fluid quality on the thermal efficiency of the ORC system is the same as the SF system. When the quality of the heat-carrying fluid is fixed, the heat-carrying fluid density and mass flow rate are constant. The specific exergy of the heat-carrying fluid increases with the rising heat-carrying fluid temperature. Therefore, the exergy efficiency of the ORC system is positively correlated with the heat-carrying fluid temperature. The increase in the quality of the heat-carrying fluid reduces the mass flow rate and specific exergy. As a result, the heat-carrying fluid quality is negatively correlated with the exergy efficiency of the ORC system.

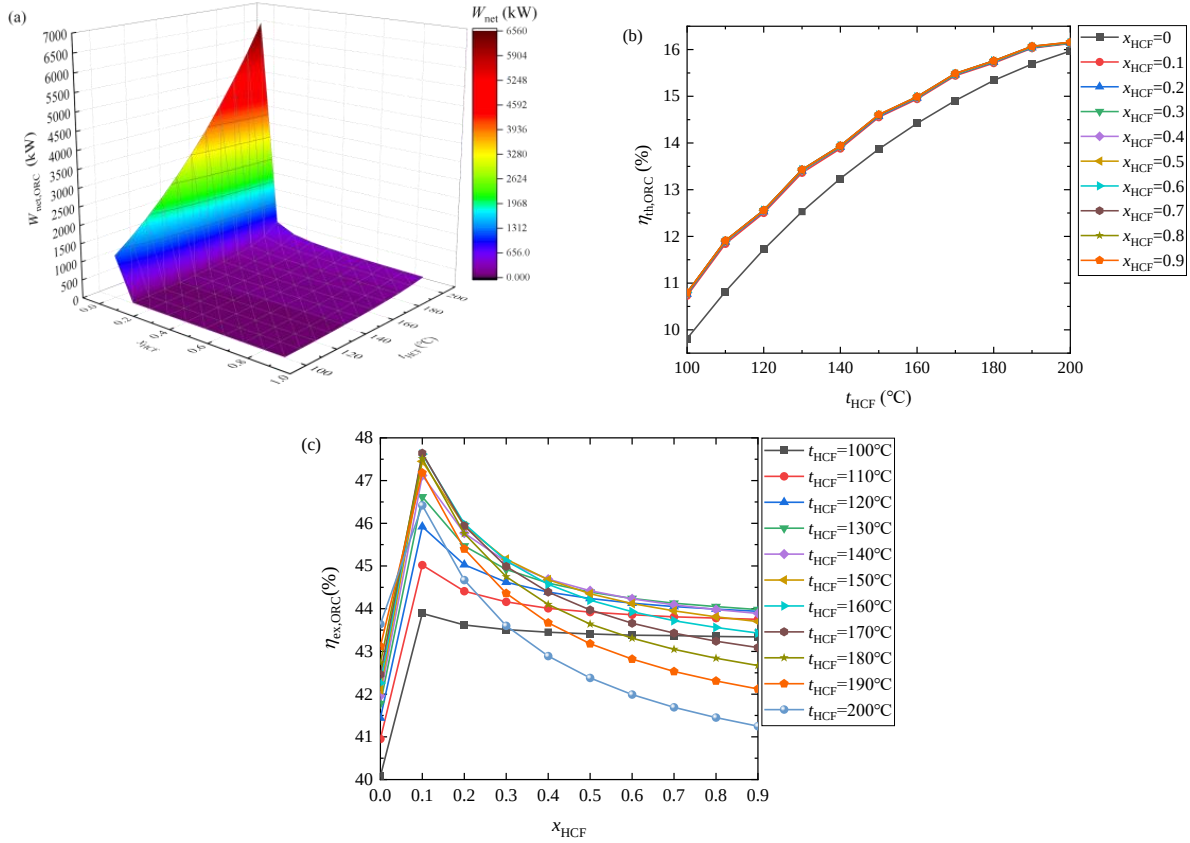


Figure 17. Variation of optimal thermodynamic parameters of the ORC system with steam quality at different heat carrier temperatures: (**a**) $W_{net,\,ORC}$, (**b**) $\eta_{th,\,ORC}$ and (**c**) $\eta_{ex,\,ORC}$.

The variation curves of the optimal thermodynamic parameters of the SFORC for different heat-carrying fluid temperatures and different steam quality are shown in Figure 18. In Figure 18a, the net power output is positively correlated with the temperature of the heat-carrying fluid and negatively correlated with the steam quality. When the heat-carrying fluid temperature is 200 °C, the steam quality changes from 0 to 0.1, and the net power

output of the SFORC system decreases from 7251 kW to 954.6 kW, which is decreased by 86.8%. The quality changes from 0.1 to 0.2, the net power output decreases by 25.9%, the steam quality changes from 0.2 to 0.3, and the net power output decreases by 12.3%. When the steam quality is greater than 0.3, the net power output of the SFORC system is reduced by about 10% for every 0.1 increment in quality, and the greater the steam quality, the lower the reduction rate of the net power output. The change in quality affects the density of the heat-carrying fluid, and as the quality increases, the rate of change in density gradually decreases, which makes the rate of decline in the net power output of the SFORC gradually decrease. As shown in Figure 18b, the thermal efficiency of the SFORC is positively correlated with the temperature and quality of the heat-carrying fluid. The difference in the thermal efficiency of the SFORC is smaller when steam quality is from 0.1 to 0.9, and the thermal efficiency corresponding to the steam quality, which is from 0.1 to 0.9, is significantly lower than that of 0 because the optimal flash temperature is lower at a steam quality of 0, which, in turn, increases the enthalpy difference between the inlet and outlet of the heat-carrying fluid. The thermal efficiency of the SFORC at the steam quality of 0 is minimal. Figure 18c displays the variation curves of the SFORC exergy efficiency. When the steam quality is from 0 to 0.3, there is maximum exergy efficiency as the heat-carrying fluid temperature increases, while when the steam quality is from 0.4 to 0.9, the exergy efficiency keeps increasing with the temperature of the heat-carrying fluid. When the steam quality is from 0 to 0.3, both the exergy utilized by the SFORC system and the net power output gradually increases with a different growth rate as the temperature of the heat-carrying fluid rises, and therefore, the extreme values of exergy appear.

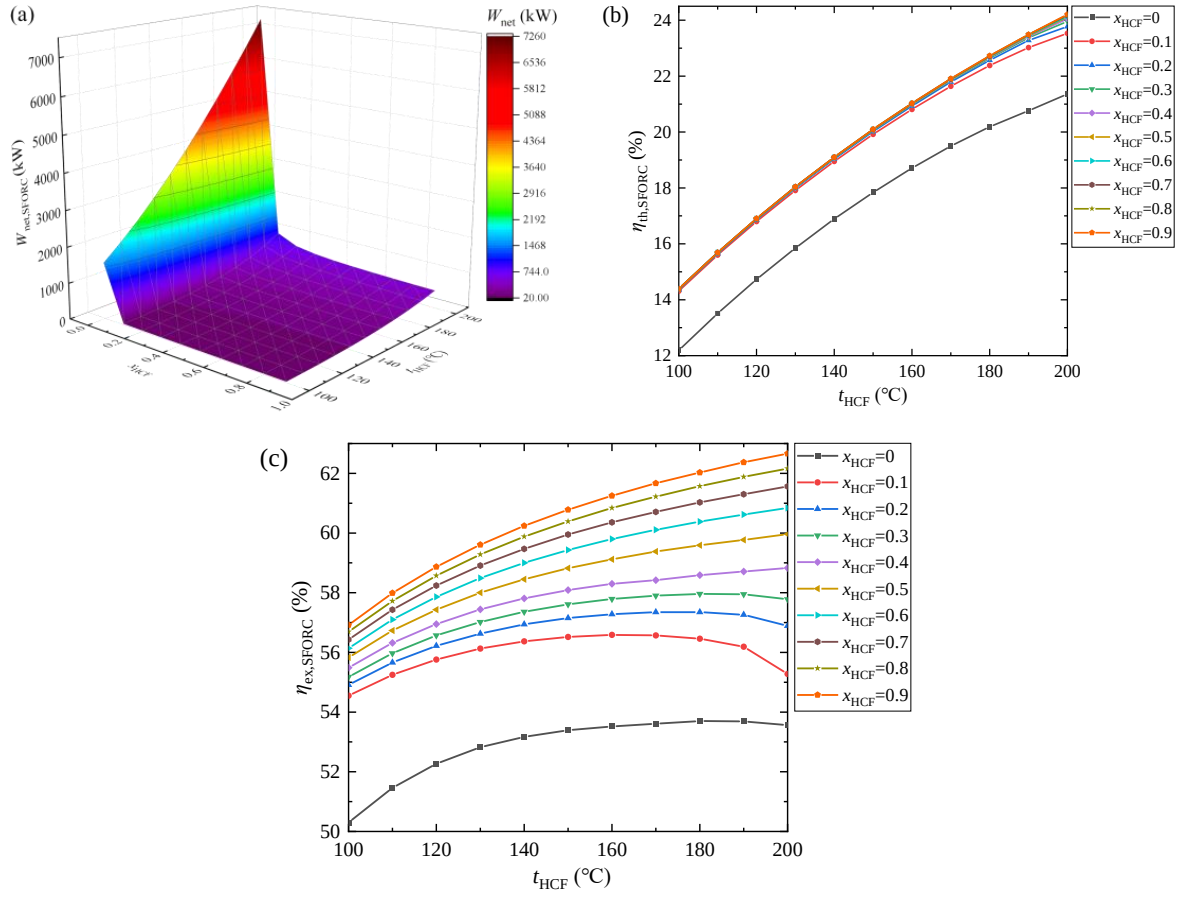


Figure 18. Variation of optimal thermodynamic parameters of the SFORC system with steam quality at different heat carrier temperatures: (**a**) $W_{net,\ SFORC}$, (**b**) $\eta_{th,\ SFORC}$ and (**c**) $\eta_{ex,\ SFORC}$.

5.3.2. Effect of Non-Condensable Gas on System Performance

The effect of different heat-carrying fluid temperatures and non-condensable gas content on the optimal thermal parameters of the SF system, the ORC system, and the SFORC system are discussed, respectively, in this chapter with the steam quality set as 0.5.

Figure 19 displays the variation curves of the optimal thermodynamic parameters of the SF system with R_{CO2} at different heat-carrying fluid temperatures. As shown in Figure 19a, the net power output is positively correlated with the heat-carrying fluid temperature, while R_{CO2} has a smaller negative impact on the net power output. The mass flow rate of the heat-carrying fluid is small for large R_{CO2}. Meanwhile, the specific enthalpy difference between the evaporator inlet and outlet of the mixture of CO_2 and heat-carrying fluid is less than that of the single geothermal water. For the SF system, the net power output reaches a maximum value of 451.4 kW at a heat-carrying fluid temperature of 200 °C and R_{CO2} of 0. The variation curves of the thermal efficiency and the exergy efficiency of the SF system are shown in Figure 19b,c. The thermal efficiency and R_{CO2} are positively correlated, while the exergy efficiency and R_{CO2} are negative correlations. The existence of non-condensable gas reduces the energy and exergy of the heat-carrying fluid available to the system. For thermal efficiency, the rate of reduction of the energy entering the system is greater than the rate of reduction of the net output power, resulting in an increasing trend, while the reduction rate of the exergy is smaller than the reduction rate of the net output power, which makes the exergy efficiency positively correlate with the net power output. The maximum thermal efficiency and the exergy efficiency are both achieved at a heat-carrying fluid temperature of 200 °C with 21.83% and 53.99%, respectively.

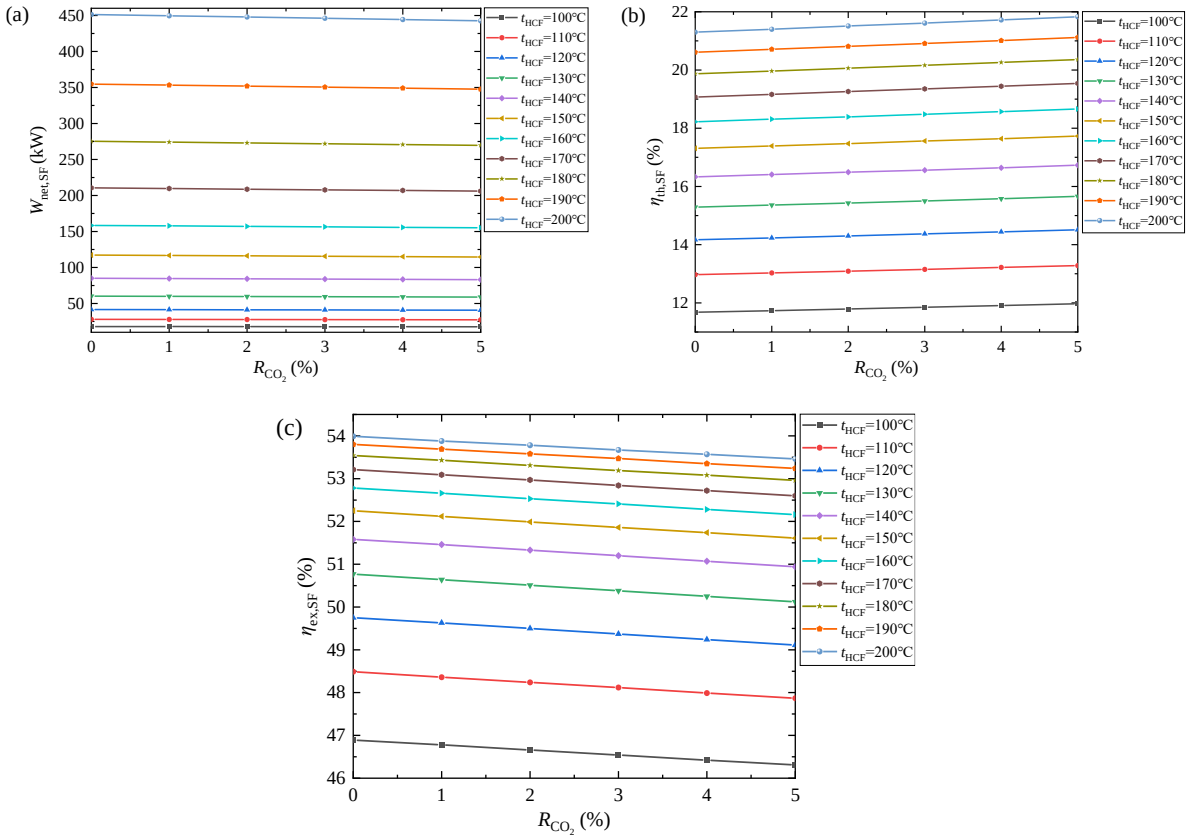


Figure 19. Variation of optimal thermodynamic parameters of the SF system with R_{CO2} at different heat carrier temperatures: (**a**) $W_{net,\,SF}$, (**b**) $\eta_{th,\,SF}$ and (**c**) $\eta_{ex,\,SF}$.

Figure 20 shows the variation curves of the optimal thermodynamic parameters of the ORC system with R_{CO2} at different heat-carrying fluid temperatures. The increase in R_{CO2} reduces the mass flow rate of the heat-carrying fluid. The net power output is

negatively correlated with R_{CO2} when the heat-carrying fluid temperature keeps fixed. The higher heat-carrying fluid temperature implies higher enthalpy utilized by the ORC system. Therefore, at a certain R_{CO2}, the correlation between the temperature of the heat-carrying fluid and the net power output of the ORC system is positive. The energy efficiency depends on the rate of change in the power output of the ORC system and thermal energy utilized concerning each other; likewise, the relative change in the net power output and exergy gained affects the increase or decrease in exergy efficiency. When the relative changes of the two are synchronized, both energy efficiency and exergy efficiency are approximately constant; this is how R_{CO2} affects energy or exergy efficiency. Contrary to that, the effect of heat-carrying fluid temperature on efficiencies is usually positive.

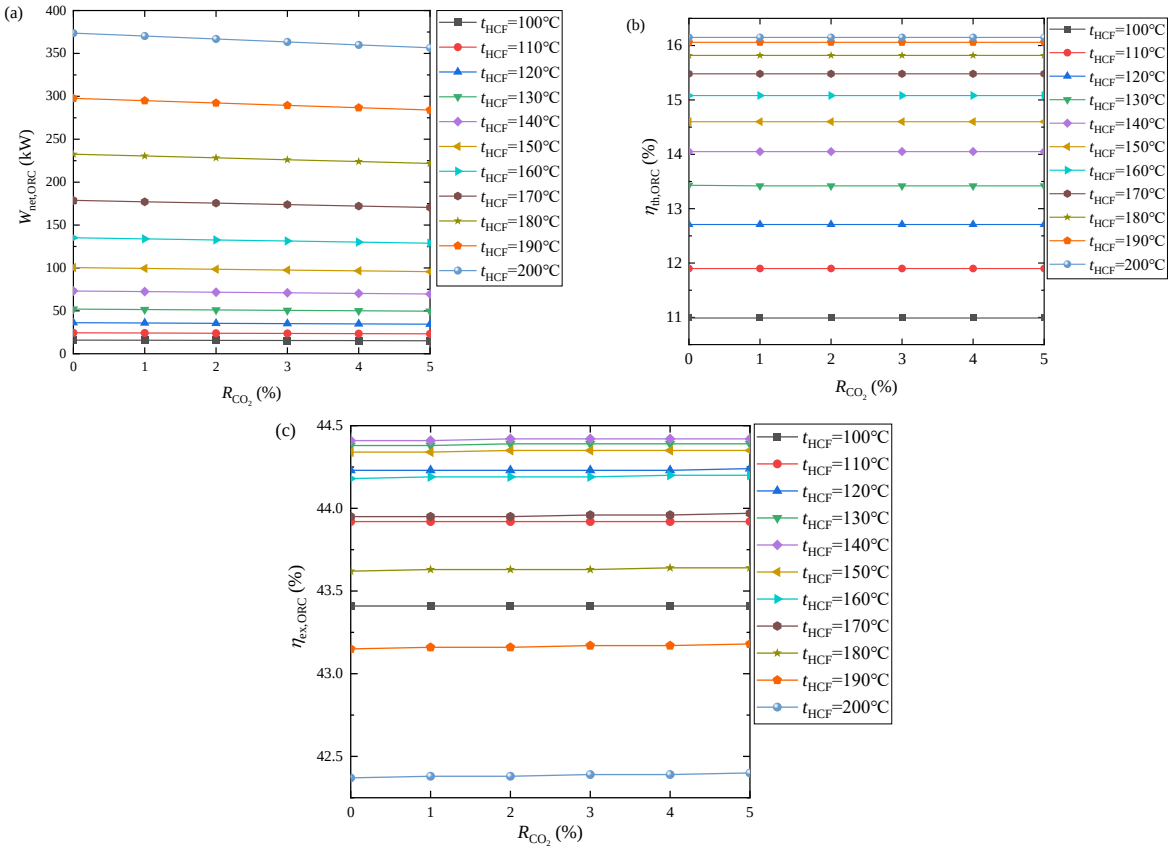


Figure 20. Variation of optimal thermodynamic parameters of the ORC system with R_{CO2} at different heat carrier temperatures: (**a**) $W_{net,\,ORC}$, (**b**) $\eta_{th,\,ORC}$ and (**c**) $\eta_{ex,\,ORC}$.

The variation curves of the optimal thermodynamic parameters of the SFORC system with R_{CO2} at different heat-carrying fluid temperatures are shown in Figure 21. The correlation between the thermodynamic parameters of the SFORC system and both the temperature and R_{CO2} of the heat-carrying fluid is similar to the SF system. The influence of non-condensable gas on the flash generation process is greater, while the influence on the mass flow rate of generated liquid heat-carrying fluid is smaller, which is used as the heat source for the ORC system. Therefore, the system performance of the SFORC system has improved relative to the SF system, but the improvement is slight. When the heat-carrying fluid temperature is 200 °C and R_{CO2} is 0, the net power output reaches the maximum which is 557.2 kW, and the maximum of exergy efficiency is 60.13%, while the maximum thermal efficiency is 24.11% when R_{CO2} equals 5%.

After the heat-carrying fluid is flashing, all that enters the SF system, the ORC subsystem and the SF subsystem of the SFORC system is single-phase fluid, and there is no violent phase change of the heat-carrying fluid during the heat transfer process. The state of the heat source corresponding to the pinch point is easy to determine. In contrast, the

heat-carrying fluid undergoes a violent phase change during the heat transfer process in the ORC system, and it is difficult to establish the state of the heat source corresponding to the pinch point and the optimal mass flow rate of the working fluid. In previous studies on phase change heat transfer, reasonable data are usually obtained by assuming the temperature of the heat-carrying fluid at the outlet and performing lots of iterations [53]. Although the error of the mathematical model is not negligible, the conclusion is still reasonable by comparing the effect of R_{CO2} on the three systems, which is that the effect of R_{CO2} on the net power output is negative, while the presence of small amounts of non-condensable gas has only a minor effect on efficiency.

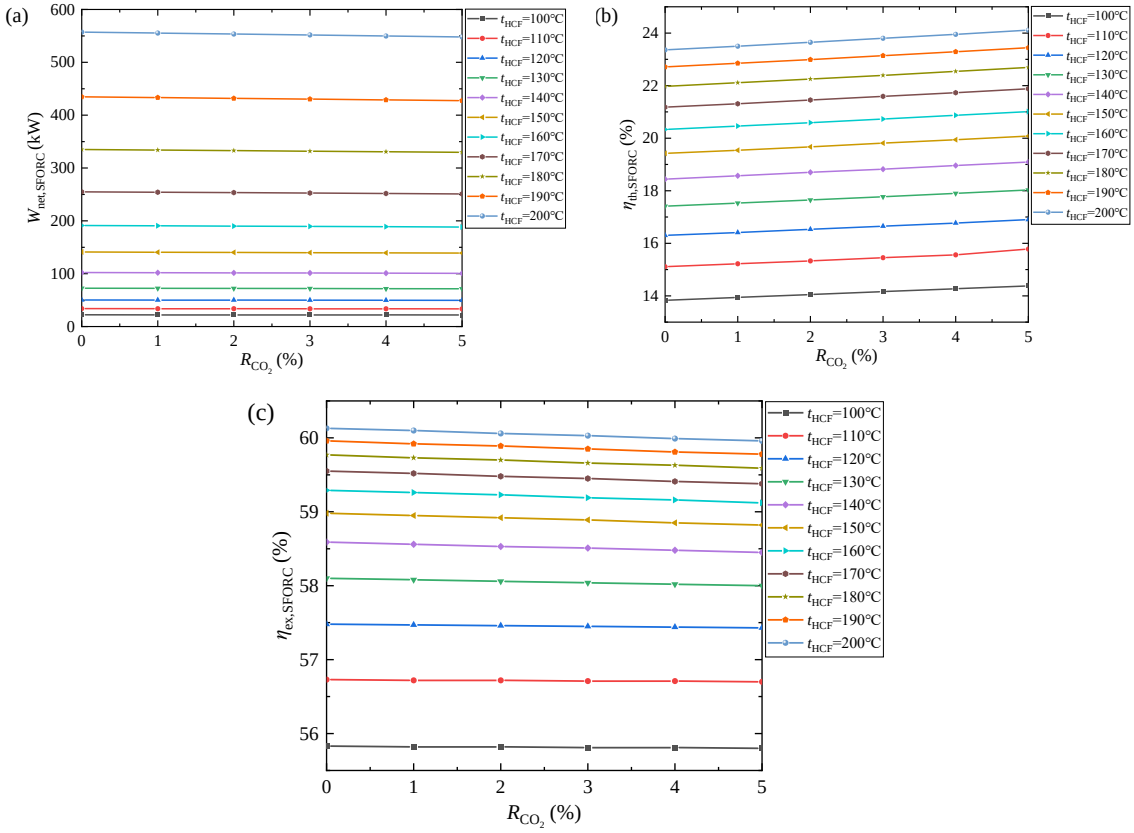


Figure 21. Variation of optimal thermodynamic parameters of the SFORC system with R_{CO2} at different heat carrier temperatures: (**a**) $W_{net,\ SFORC}$, (**b**) $\eta_{th,\ SFORC}$ and (**c**) $\eta_{ex,\ SFORC}$.

Especially considering the specific situation of the geothermal hot dry rock resources in China, in which the steam quality and NCG content of the heat-carrying fluid is relatively lower, it seems that the three systems can all be applied. In heat exchanger designs, heat-carrying fluids are often simplified to pure water, and the ORC is not well-adapted to steam quality changes which affect where the pinch point of heat transfer occurs in the evaporator. NCG must be separated efficiently in the SF system and the SFORC system because its presence is always harmful, while the separation of NCG can be ignored in the ORC system. To sum up, for geothermal energy conversion systems in China, the SFORC system is more recommended, the ORC system is second, and the SF system is worse.

6. Conclusions

Based on the thermodynamics model, the synergetic effect of steam quality and non-condensable gas (NCG) on production capacity testing and energy conversion system optimization is investigated in this paper. The energy conversion systems include a single flash (SF) system, an organic Rankine cycle (ORC) system and a single flash combined organic Rankine cycle (SFORC) system. The main conclusions of this paper are summarized as follows:

1. Steam quality should be considered in production capacity testing and adapted to geothermal power stations in engineering applications. The presence of NCG is always harmful.
2. The increment of steam quality causes an upward shift in the optimal evaporation/flash temperature, while the NCG content has less effect on the optimal evaporation/flash temperature.
3. For heat-carrying two-phase fluids, the SFORC system has a better overall performance than the SF system and the ORC system, while the ORC system is recommended in the case of a higher NCG content.
4. Especially considering the specific situation of the hot dry rock resources in China, the SFORC system is the better choice.

Author Contributions: Formal analysis, R.G.; Investigation, Q.L.; Methodology, T.L.; Supervision, T.L.; Writing—original draft, R.G.; Writing—review & editing, X.G. All authors have read and agreed to the published version of the manuscript.

Funding: The authors gratefully acknowledge the support provided by the National Natural Science Foundation of China (Grant No. 52176183).

Institutional Review Board Statement: Not applicable.

Informed Consent Statement: Not applicable.

Data Availability Statement: Not applicable.

Conflicts of Interest: The authors declare no conflict of interest.

Nomenclature

General		*Subscript*	
t	temperature (°C)	HCF	heat-carrying fluid
P	pressure	net	net output
m	mass flow rate (kg/s)	E	evaporator
V	volume flow rate (m^3/s)	T	turbine
h	specific enthalpy (kJ/kg)	C	condenser
H	enthalpy (kJ)	P	pump
H	head (m)	G	generator
x	quality	wf	working fluid
ex	specific exergy (kJ/kg)	hp	heat-carrying fluid pump
EX	exergy (kJ)	cp	cooling water pump
R	volume rate (%)	w	geothermal water
W	work (kW)	s	geothermal steam
Q	heat exchange (kW)	in	inlet
c	specific heat capacity (kJ/(kg·K))	out	outlet
s	specific entropy	0	ambient state
SF	single flash system	1–13	state point
ORC	organic Rankine cycle	cw	cooling water
SFORC	single flash combined organic Rankine cycle system	pp	pinch point
HDR	hot dry rock	F	flash evaporator
EGS	enhanced geothermal system	e	evaporation
NCG	non-condensable gas	c	condense
g	Spend of gravity (m/s^2)	th	thermal
ODP	ozone depletion potential	m	mechanical transmission
GWP	global warming potential	f	flash
Greek			
ρ	density (kg/m^3)		
η	efficiency (%)		

References

1. He, J.-K. Objectives and strategies for energy revolution in the context of tackling climate change. *Adv. Clim. Chang. Res.* **2015**, *6*, 101–107. [CrossRef]
2. Liu, X.; Wei, M.; Yang, L.; Wang, X. Thermo-economic analysis and optimization selection of ORC system configurations for low temperature binary-cycle geothermal plant. *Appl. Therm. Eng.* **2017**, *125*, 153–164. [CrossRef]
3. Alegria, P.; Catalan, L.; Araiz, M.; Rodriguez, A.; Astrain, D. Experimental development of a novel thermoelectric generator without moving parts to harness shallow hot dry rock fields. *Appl. Therm. Eng.* **2022**, *200*, 117619. [CrossRef]
4. Olasolo, P.; Juárez, M.C.; Olasolo, J.; Morales, M.P.; Valdani, D. Economic analysis of Enhanced Geothermal Systems (EGS). A review of software packages for estimating and simulating costs. *Appl. Therm. Eng.* **2016**, *104*, 647–658. [CrossRef]
5. Lacirignola, M.; Blanc, I. Environmental analysis of practical design options for enhanced geothermal systems (EGS) through life-cycle assessment. *Renew. Energy* **2013**, *50*, 901–914. [CrossRef]
6. Bataillé, A.; Genthon, P.; Rabinowicz, M.; Fritz, B. Modeling the coupling between free and forced convection in a vertical permeable slot: Implications for the heat production of an Enhanced Geothermal System. *Geothermics* **2006**, *35*, 654–682. [CrossRef]
7. Lu, S.-M. A global review of enhanced geothermal system (EGS). *Renew. Sustain. Energy Rev.* **2018**, *81*, 2902–2921. [CrossRef]
8. Olasolo, P.; Juárez, M.C.; Morales, M.P.; D'Amico, S.; Liarte, I.A. Enhanced geothermal systems (EGS): A review. *Renew. Sustain. Energy Rev.* **2016**, *56*, 133–144. [CrossRef]
9. Sun, F.; Yao, Y.; Li, G.; Li, X. Geothermal energy development by circulating CO2 in a U-shaped closed loop geothermal system. *Energy Convers. Manag.* **2018**, *174*, 971–982. [CrossRef]
10. Loni, R.; Mahian, O.; Najafi, G.; Sahin, A.Z.; Rajaee, F.; Kasaeian, A.; Mehrpooya, M.; Bellos, E.; le Roux, W.G. A critical review of power generation using geothermal-driven organic Rankine cycle. *Therm. Sci. Eng. Prog.* **2021**, *25*, 101028. [CrossRef]
11. Desideri, U.; Bidini, G. Study of possible optimisation criteria for geothermal power plants. *Energy Convers. Manag.* **1997**, *38*, 1681–1691. [CrossRef]
12. Garg, P.; Kumar, P.; Srinivasan, K.; Dutta, P. Evaluation of isopentane, R-245fa and their mixtures as working fluids for organic Rankine cycles. *Appl. Therm. Eng.* **2013**, *51*, 292–300. [CrossRef]
13. Hu, D.; Li, S.; Zheng, Y.; Wang, J.; Dai, Y. Preliminary design and off-design performance analysis of an Organic Rankine Cycle for geothermal sources. *Energy Convers. Manag.* **2015**, *96*, 175–187. [CrossRef]
14. Alimonti, C.; Conti, P.; Soldo, E. A comprehensive exergy evaluation of a deep borehole heat exchanger coupled with a ORC plant: The case study of Campi Flegrei. *Energy* **2019**, *189*, 110160. [CrossRef]
15. Wang, Y.; Li, C.; Zhao, J.; Wu, B.; Du, Y.; Zhang, J.; Zhu, Y. The above-ground strategies to approach the goal of geothermal power generation in China: State of art and future researches. *Renew. Sustain. Energy Rev.* **2021**, *138*, 110557. [CrossRef]
16. Klein, C.W.; Chase, D.; Geothermal Resources, C. Chemical transients during production of high gas wells at the northern Geysers steam field, California, USA. In Proceedings of the 1995 Annual Meeting of the Geothermal-Resources-Council, Accomplishments of the Past and Challenges of the Future, Reno, NV, USA, 8–11 October 1995; pp. 513–519.
17. Kaya, E.; Zarrouk, S.J. Reinjection of greenhouse gases into geothermal reservoirs. *Int. J. Greenh. Gas Control* **2017**, *67*, 111–129. [CrossRef]
18. Nogara, J.; Zarrouk, S.J.; Seastres, J. Surface analysis of metal alloys exposed to geothermal fluids with high non-condensable gas content. *Geothermics* **2018**, *72*, 372–399. [CrossRef]
19. Gunerhan, G.G. An upstream reboiler design for removal of noncondensable gases from geothermal steam for Kizildere geothermal power plant, Turkey. *Geothermics* **1999**, *28*, 739–757. [CrossRef]
20. Mubarok, M.H.; Cater, J.E.; Zarrouk, S.J. Comparative CFD modelling of pressure differential flow meters for measuring two-phase geothermal fluid flow. *Geothermics* **2020**, *86*, 101801. [CrossRef]
21. Mubarok, M.H.; Zarrouk, S.J.; Cater, J.E.; Mundakir, A.; Bramantyo, E.A.; Lim, Y.W. Real-time enthalpy measurement of two-phase geothermal fluid flow using load cell sensors: Field testing results. *Geothermics* **2021**, *89*, 101930. [CrossRef]
22. Hasan, A.R.; Kabir, C.S. Modeling two-phase fluid and heat flows in geothermal wells. *J. Pet. Sci. Eng.* **2010**, *71*, 77–86. [CrossRef]
23. Karabacak, R.; Mücasiroğlu, F.; Tan, M.; Karabacak, S. Research of production of CO_2 from non-condensable gases in geothermal fluid and cost analysis. *Geothermics* **2017**, *68*, 1–8. [CrossRef]
24. Manente, G.; Bardi, A.; Lazzaretto, A.; Paci, M. Low emission flash-binary and two-phase binary geothermal power plants with water absorption and reinjection of non-condensable gases. *Geothermics* **2019**, *80*, 155–169. [CrossRef]
25. Altar, D.E.; Kaya, E. Numerical modelling of the interaction between geothermal injectate-non condensable gas solutions and greywacke. *Int. J. Greenh. Gas Control* **2020**, *94*, 102922. [CrossRef]
26. Ayachi, F.; Boulawz Ksayer, E.; Zoughaib, A.; Neveu, P. ORC optimization for medium grade heat recovery. *Energy* **2014**, *68*, 47–56. [CrossRef]
27. Quoilin, S.; Declaye, S.; Tchanche, B.F.; Lemort, V. Thermo-economic optimization of waste heat recovery Organic Rankine Cycles. *Appl. Therm. Eng.* **2011**, *31*, 2885–2893. [CrossRef]
28. Pambudi, N.A.; Itoi, R.; Jalilinasrabady, S.; Jaelani, K. Exergy analysis and optimization of Dieng single-flash geothermal power plant. *Energy Convers. Manag.* **2014**, *78*, 405–411. [CrossRef]

29. Rudiyanto, B.; Bahthiyar, M.A.; Pambudi, N.A.; Widjonarko; Hijriawan, M. An update of second law analysis and optimization of a single-flash geothermal power plant in Dieng, Indonesia. *Geothermics* **2021**, *96*, 102212. [CrossRef]
30. Dagdas, A. Performance analysis and optimization of double-flash geothermal power plants. *J. Energy Resour. Technol.-Trans. ASME* **2007**, *129*, 125–133. [CrossRef]
31. Pambudi, N.A.; Itoi, R.; Jalilinasrabady, S.; Jaelani, K. Performance improvement of a single-flash geothermal power plant in Dieng, Indonesia, upon conversion to a double-flash system using thermodynamic analysis. *Renew. Energy* **2015**, *80*, 424–431. [CrossRef]
32. Meng, N.; Li, T.; Wang, J.; Jia, Y.; Liu, Q.; Qin, H. Synergetic mechanism of fracture properties and system configuration on techno-economic performance of enhanced geothermal system for power generation during life cycle. *Renew. Energy* **2020**, *152*, 910–924. [CrossRef]
33. Abdolalipouradl, M.; Mohammadkhani, F.; Khalilarya, S. A comparative analysis of novel combined flash-binary cycles for Sabalan geothermal wells: Thermodynamic and exergoeconomic viewpoints. *Energy* **2020**, *209*, 118235. [CrossRef]
34. Fang, Y.; Yang, F.; Zhang, H. Comparative analysis and multi-objective optimization of organic Rankine cycle (ORC) using pure working fluids and their zeotropic mixtures for diesel engine waste heat recovery. *Appl. Therm. Eng.* **2019**, *157*, 113704. [CrossRef]
35. Wang, H.; Li, H.; Wang, L.; Bu, X. Thermodynamic Analysis of Organic Rankine Cycle with Hydrofluoroethers as Working Fluids. In Proceedings of the 8th International Conference on Applied Energy (ICAE2016), Beijing, China, 8–11 October 2017; pp. 1889–1894.
36. Hung, T.C.; Wang, S.K.; Kuo, C.H.; Pei, B.S.; Tsai, K.F. A study of organic working fluids on system efficiency of an ORC using low-grade energy sources. *Energy* **2010**, *35*, 1403–1411. [CrossRef]
37. Li, T.; Zhang, Z.; Lu, J.; Yang, J.; Hu, Y. Two-stage evaporation strategy to improve system performance for organic Rankine cycle. *Appl. Energy* **2015**, *150*, 323–334. [CrossRef]
38. Dawo, F.; Fleischmann, J.; Kaufmann, F.; Schifflechner, C.; Eyerer, S.; Wieland, C.; Spliethoff, H. R1224yd(Z), R1233zd(E) and R1336mzz(Z) as replacements for R245fa: Experimental performance, interaction with lubricants and environmental impact. *Appl. Energy* **2021**, *288*, 116661. [CrossRef]
39. Aali, A.; Pourmahmoud, N.; Zare, V. Exergoeconomic analysis and multi-objective optimization of a novel combined flash-binary cycle for Sabalan geothermal power plant in Iran. *Energy Convers. Manag.* **2017**, *143*, 377–390. [CrossRef]
40. Shokati, N.; Ranjbar, F.; Yari, M. Comparative and parametric study of double flash and single flash/ORC combined cycles based on exergoeconomic criteria. *Appl. Therm. Eng.* **2015**, *91*, 479–495. [CrossRef]
41. Shamoushaki, M.; Fiaschi, D.; Manfrida, G.; Talluri, L. Energy, exergy, economic and environmental (4E) analyses of a geothermal power plant with NCGs reinjection. *Energy* **2022**, *244*, 122678. [CrossRef]
42. Chen, C.; Witte, F.; Tuschy, I.; Kolditz, O.; Shao, H. Parametric optimization and comparative study of an organic Rankine cycle power plant for two-phase geothermal sources. *Energy* **2022**, *252*, 123910. [CrossRef]
43. Li, T.; Liu, Q.; Gao, X.; Meng, N.; Kong, X. Thermodynamic, economic, and environmental performance comparison of typical geothermal power generation systems driven by hot dry rock. *Energy Rep.* **2022**, *8*, 2762–2777. [CrossRef]
44. Li, H.; Cao, F.; Bu, X.; Wang, L.; Wang, X. Performance characteristics of R1234yf ejector-expansion refrigeration cycle. *Appl. Energy* **2014**, *121*, 96–103. [CrossRef]
45. Liu, X.; Li, H.; Bu, X.; Wang, L.; Xie, N.; Zeng, J. Performance characteristics and working fluid selection for low-temperature binary-flashing cycle. *Appl. Therm. Eng.* **2018**, *141*, 51–60. [CrossRef]
46. DiPippo, R. Geothermal double-flash plant with interstage reheating: An updated and expanded thermal and exergetic analysis and optimization. *Geothermics* **2013**, *48*, 121–131. [CrossRef]
47. Mohammadzadeh Bina, S.; Jalilinasrabady, S.; Fujii, H. Exergoeconomic analysis and optimization of single and double flash cycles for Sabalan geothermal power plant. *Geothermics* **2018**, *72*, 74–82. [CrossRef]
48. Fan, G.; Gao, Y.; Ayed, H.; Marzouki, R.; Aryanfar, Y.; Jarad, F.; Guo, P. Energy and exergy and economic (3E) analysis of a two-stage organic Rankine cycle for single flash geothermal power plant exhaust exergy recovery. *Case Stud. Therm. Eng.* **2021**, *28*, 101554. [CrossRef]
49. Saleh, B.; Koglbauer, G.; Wendland, M.; Fischer, J. Working fluids for low-temperature organic Rankine cycles. *Energy* **2007**, *32*, 1210–1221. [CrossRef]
50. Liu, G.; Zhou, C.; Liao, S. Comparative study on heat extraction performance between gravity heat pipe system and enhanced geothermal system. *Geothermics* **2021**, *96*, 102218. [CrossRef]
51. Li, T.; Gao, R.; Gao, X. Energy, exergy, economic, and environment (4E) assessment of trans-critical organic Rankine cycle for combined heating and power in wastewater treatment plant. *Energy Convers. Manag.* **2022**, *267*, 115932. [CrossRef]
52. Sulaiman, A.Y.; Cotter, D.F.; Le, K.X.; Huang, M.J.; Hewitt, N.J. Thermodynamic analysis of subcritical High-Temperature heat pump using low GWP Refrigerants: A theoretical evaluation. *Energy Convers. Manag.* **2022**, *268*, 116034. [CrossRef]
53. Roy, S.; Maiya, M.P. Analysis of pinch point in liquid–vapour heat exchanger of R134a–DMAC vapour absorption refrigeration system. *Appl. Therm. Eng.* **2013**, *50*, 1619–1626. [CrossRef]